# Measurement of neutron elastic scattering cross sections for $^{12}$C, $^{40}$Ca, and $^{208}$Pb at energies from 65 to 225 MeV

J. H. Osborne,* F. P. Brady, and J. L. Romero
*University of California, Davis, California 95616, USA*

J. L. Ullmann, D. S. Sorenson, A. Ling,† N. S. P. King, and R. C. Haight
*Los Alamos National Laboratory, Los Alamos, New Mexico 87545, USA*

J. Rapaport and R. W. Finlay
*Ohio University, Athens, Ohio 45701, USA*

E. Bauge and J. P. Delaroche
*Commissariat à l'Energie Atomique, Bruyères-le-Châtel, France*

A. J. Koning
*Nuclear Research and Consulting Group, Petten, The Netherlands*
(Received 11 June 2004; published 29 November 2004)

Differential neutron elastic scattering cross sections for $^{12}$C, $^{40}$Ca, and $^{208}$Pb have been measured using the continuum neutron source at the Los Alamos Neutron Science Center. The mean incident neutron kinetic energies ranged from 65 to 225 MeV. The large acceptance drift chamber based $(n,p)$ recoil detector telescope spanned a center-of-mass angular range of 7° to 23°. The measured cross sections are compared with calculations obtained with different optical model potentials, including predictions based on microscopic theory and phenomenology.

DOI: 10.1103/PhysRevC.70.054613 PACS number(s): 25.75.Dw

## I. INTRODUCTION

Understanding the nucleon-nucleus interaction has been one of the long term goals of nuclear physics [1]. One important experimental method for exploring this interaction is to scatter nucleons off various nuclei over a range of energies, thus varying the sensitivity to different terms in the interaction, which is often described by a potential [2]. These measurements are then compared to the results predicted by different models of the nuclear potential or can be used to help construct a potential. There have been many measurements of proton-nucleus scattering, but few of neutron scattering at these energies. Those of Hjort *et al.* at 65 MeV [3], Salmon at 96 MeV [4], and from the Uppsala facility [5–7], also at 96 MeV, are the most recent. Aside from these there are only a handful of higher energy data points at a few energies [8–11]. Here we overlap the 65 MeV data and provide an extensive set of neutron elastic data at higher energies, which can be compared to the relativistic and nonrelativistic models available. There is also practical interest in the use of such models in applications such as nuclear medicine, nuclear energy, waste transmutation, and radiation effects on electronics.

A common basis for many models of the nuclear potential is the optical model potential (OMP) whose basic form is shown in Eq. (1). The $V(E,r)$ term can then be further subdivided as in Eq. (2) where $V_C(r)$ is the Coulomb term, $V_{so}(E,r)$ is the spin-orbit interaction term, and $R$ and $a$ are adjustable radius and diffuseness parameters of the Woods-Saxon form.

$$U(E,r) = V(E,r) + iW(E,r), \tag{1}$$

$$V(E,r) = V_C(r) + V_{so}(E,r) + \frac{V(E)}{1+\exp[(r-R)/a]}. \tag{2}$$

$V(E)$ is the projectile lab energy dependence of the potential and its form is shown in Eq. (3) [12], where **t** is the isospin of the incident particle, **T** is the isospin of the target, and $\Delta V_C$ is the Coulomb correction term. $\Delta V_C$ is approximately equal to $0.4(Z/A^{1/3})$ MeV [13].

$$V(E) = V_0(E) + (4/A)V_1(E)\mathbf{t}\cdot\mathbf{T} + \Delta V_C. \tag{3}$$

The difference between proton-nucleus and neutron-nucleus scattering will show up in the diagonal elements of the $\mathbf{t}\cdot\mathbf{T}$ matrix. The magnitude of the Coulomb correction term can, in principle, be determined by comparing neutron and proton scattering from the same $T=0$ nucleus. This has been accomplished at low energy [14–18]. But the lack of neutron scattering data at higher energies has inhibited determination of this term of the nuclear potential in this energy region.

In this paper we report neutron elastic cross sections for two such $N=Z$ nuclei, $^{12}$C and $^{40}$Ca. However, experimental uncertainties in the data did not allow an independent deter-

*Present address: California State University, Sacramento, California, USA.

†Present address: Redex Corporation, Bedford, Massachusetts, USA.

 ©2004 The American Physical Society

mination of $\Delta V_C$, and the value $0.4(Z/A^{1/3})$ is used [13]. Nor did we attempt an analysis to see if $V_1$ could be determined. Again, at low energies this has been done [19,12], but it was not possible here due to the uncertainties in the present $^{208}$Pb$(n,n)$ data. The energy dependence of the OMP parameters has been a subject of considerable interest [2,7]. However, there are no data reported on a systematic study of the energy dependence of neutron elastic scattering differential cross section. In this paper we present the first data of this kind at neutron energies from 65 to 225 MeV. This work used the unmoderated continuum energy neutron beam at LAMPF [now the Los Alamos Neutron Science Center (LANSCE)]. The elastic data have been combined into ten bins with mean incident energies from 65 to 225 MeV, for angles from 7° to 23° and for target nuclei of $^{12}$C, $^{40}$Ca, and $^{208}$Pb; e.g., beam neutrons from 60 to 70 MeV constitute the 65 MeV bin.

## II. EXPERIMENTAL METHOD

### A. Overview

This experiment was performed at the flight path 4FP15L at the WNR facility of the Los Alamos Neutron Science Center [20]. For this experiment the LAMPF accelerator provided a pulsed 800 MeV proton beam to the WNR where it collided with a 7.5 cm long, 3.0 cm diameter tungsten target. The typical proton beam time structure consisted of micropulses of approximately 230 ps full width at half maximum (FWHM) separated by 1.8 $\mu$s inside a macropulse 640 $\mu$s long. The macropulse frequency was typically 100 Hz. Neutrons are produced at a continuum of energies up to 800 MeV. These are collimated in a 90 *m* flight path to the experimental area. Absorbers of $CH_2$ (5.08 cm thick) and $^{nat}$Pb (2.54 cm) were inserted in the beam just downstream of the shutter to reduce the number of low energy neutrons and gamma rays in the beam. A permanent magnet for clearing charged particles from the beam was located just downstream of the absorbers. The polarization of the beam for the 15L beamline has been measured to be about 1 (±1) % at our lowest energy (65 MeV) and near 8 (±1) % at our highest energy (225 MeV) [21].

The incident neutron energy for each event is determined by time of flight (TOF). The detection system is shown in Fig. 1, and described in detail below. Veto1 and Veto2 are wire chambers used to veto charged particles in the beam. TP is a small scintillator whose tip is inserted into the beam next to the experimental target and is used as a backup neutron beam flux monitor and for a continuous check of detector calibrations. VP is a large area scintillation paddle used to veto charged particles scattered from or produced in the target and going into the detector telescope. LC1 and LC2 are large area scintillation detectors used to convert neutrons scattered from the target to charged particles and then measure the energy deposited by those charged particles in the converter. DC3 and DC4 are drift chambers which identify the trajectory of the charged particles through the detector telescope. $\Delta E$ is a large area scintillating paddle which provided a stop signal for time-of-flight measurements and $\Delta E$ for particle identification. $E$ is an array of 15 CsI(Tl) detectors used to stop and measure the energies of the detected particles. Not shown is the fission chamber that was inserted into the beam downstream of the detection system to measure the neutron beam flux.

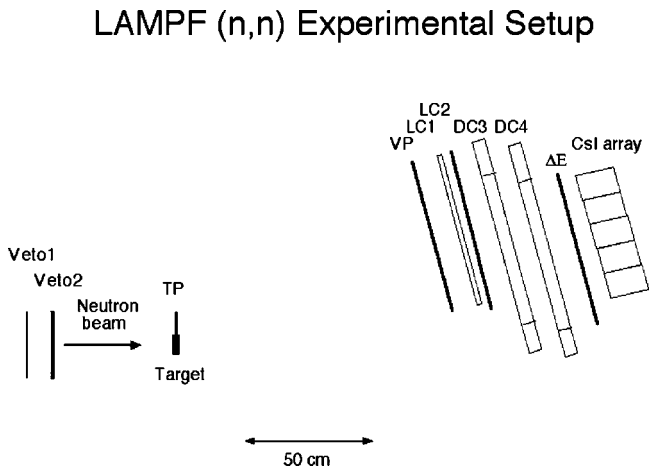


FIG. 1. Detector geometry showing the beam, target, and detection system components. See text for description of the components.

The detector setup for this experiment was based on the $(n,p)$ and $(n,n)$ detector systems designed and developed at Crocker Nuclear Laboratory (CNL) at the University of California, Davis (UC Davis) [3,22–24]. (The facility at Uppsala [5] is also modeled after the CNL/UC Davis facility.) The actual detectors used for this experiment were first developed for $(n,p)$ experiments on the WNR/LANL 15L beamline [25–27]. The new detectors for the $(n,n)$ experiment were LC1 and LC2, the live converters. The other detectors will be discussed only briefly since their construction and performance have been detailed elsewhere [26]. The design and construction of the live converters will be discussed in some detail, and more detail is given in Ref. [24].

### B. Targets

Four different scattering targets (as well as no-target runs) were used in this experiment. The $CH_2$, C, and Ca targets were cylindrical targets of natural isotopic composition (98.89% $^{12}$C and 96.97% $^{40}$Ca, respectively). The cylinders were oriented with their axes along the beam direction. The dimensions of the cylindrical targets are shown in Table I. The Pb target was 99.5% $^{208}$Pb, and composed of two rectangular pieces. The mass of one piece was 116.243 g while

TABLE I. Dimensions of cylindrical targets.

| Target | Mass (g) | Length (cm) | Diameter (cm) | Density (g/cm$^3$) | $\rho_t$ (g/cm$^2$) |
|---|---|---|---|---|---|
| $CH_2$ | 149.7 | 7.650 | 5.084 | 0.964 | 7.37 |
| $^{12}$C | 176.7 | 5.080 | 5.082 | 1.715 | 8.71 |
| $^{40}$Ca | 165.7 | 5.126 | 5.116 | 1.573 | 8.06 |

the other was 62.55 g for a total mass of 178.793 g and a thickness of 11.71 g/cm$^2$. The neutron beam was collimated to 6.5 cm$\times$7.9 cm, and all the targets were suspended in the beam by thin wires.

### C. Veto chambers

Veto1 and Veto2 are two thin multiwire proportional chambers placed in the beam upstream of the experimental target. If either chamber detects a particle, then that event is thrown out, since this indicates with high probability that a charged particle in the beam caused the event. This is a software veto. These wire chambers were previously used as target chambers in the earlier $(n,p)$ experiments on the same beamline [25]. The wire chambers have a 15.24 cm $\times$15.24 cm active area with a 4 mm wire spacing. The wires are 20 $\mu$m gold plated tungsten. Anode voltages used were close to +2200 V. Efficiencies of each were measured to be greater than 99% during the experiment.

### D. Target paddle

The target paddle (TP) was a 5.08 cm$\times$5.08 cm $\times$1.59 mm plastic scintillator. It was placed so that the tip (about 5 mm) of the scintillator was in the neutron beam next to the middle of the target. Some beam neutrons hitting this scintillator knocked out protons which then passed through the detector telescope. These $(n,p)$ events were identified by TP and VP firing and neither Veto1 or Veto2 recording a hit and were recorded using the prescaled trigger. These events allowed a continuous gain check of the CsI(Tl) detectors (along with cosmic ray events), a backup beam flux detector, and backup data for the calibration of LC1 and LC2.

### E. Veto paddle

The veto paddle (VP) was a 50.8 cm$\times$30.48 cm $\times$3.18 mm plastic scintillator. Adiabatic light pipes connected the scintillating material to photomultiplier tubes at the top and bottom of the detector. A signal in VP identified a given event as a neutron-induced charged-particle event. A lack of signal from VP was used as part of the main (scattered neutron) trigger (veto bar). This detector was previously used as a $\Delta E$ detector in the $(n,p)$ experiments. Its efficiency was measured to be greater than 99% at rates encountered in this experiment.

### F. Drift chambers

The primary purpose of the drift chambers DC3 and DC4 was to define the trajectory of the detected particle. From that trajectory, several useful quantities can be calculated. First, in the $(n,p)$ mode of operation [see Sec. II M below for a description of the $(n,p)$ and $(n,n)$ modes of operation], the trajectory identifies whether the event came from the target location and, if so, the angle of this trajectory to the beam direction defines the $(n,p)$ scattering angle. In the $(n,n)$ mode of operation, the charged-particle trajectory is used to calculate the ($n$-$p$) or ($n$-C) hit point of the event on LC1 and on LC2. This location is then used with the center of the target to calculate the $(n,n)$ scattering angle. Knowledge of the $(n,n)$ scattering angle and the trajectory allows the ($n$-$p$) conversion angle to be calculated. Also, the hit location on the LC indicates which calibration/mapping zone to use for calculating the energy deposited in the converter. The trajectory path of the charged particles also allows the $dE/dx$ energy losses in the detector system that are not measured to be calculated and an accurate flight path to be determined.

The drift chamber design was based on the detectors developed earlier for LAMPF-HRS [28–30]. The drift chambers are constructed with eight aluminum frame planes. These planes are (in order from front to back) front window, ground, $X$ anode, ground, $Y$ anode, ground, spacer, and back window planes. The two anode planes have a $30\times60$ cm$^2$ active area. Their anode wire spacing is 8 mm. They have two sets of cathode wires alternating with the anode wires in the same plane. The cathodes wire are labeled either odd or even with a 16 mm separation between even wires, a 16 mm separation between odd wires, and an 8 mm separation between odd and even wires. The reason for two sets of cathode wires is to determine on which side of an anode wire a hit occurs. All wires in a given plane are connected to a common delay line (2.5 ns/cm) which has readouts on both ends. The difference in time between the two signals on a delay line is used to calculate the wire locations. With the wire location determined, the drift time and then drift distance can be calculated. The signals from the odd and even cathodes are fed into a differential amplifier. The output of the differential amplifier is gated to distinguish the odd cathode signals from the even cathode signals. Chamber efficiencies ranged from 97% to 99.5%.

### G. $\Delta E$ detector

The $\Delta E$ detector was a 50.8 cm$\times$30.5 cm$\times$4.8 mm plastic scintillator. Adiabatic light pipes connected the scintillating material to photomultiplier tubes at the top and bottom of the detector. This detector was part of the main trigger. It supplied the start signal for the time-of-flight measurement of the neutron energy for each event and was used in conjunction with the $E$ detector for particle identification via $E-\Delta E$. The timing resolution of the $\Delta E$ detector was previously measured [26] using a source and small scintillating paddle to be about 750 ps.

### H. $E$ detector

The $E$ detector is made up of an array (wall) of 15 CsI(Tl) detectors. Each CsI(Tl) crystal has a surface area of 89 $\times$89 mm$^2$ and is 15.2 cm deep. The total surface area of the detector array is 45.1 cm$\times$27.0 cm. The CsI crystals have a higher density than NaI (4.51 versus 3.67 g/cm$^3$). This means that a smaller crystal can be used to stop a proton at a given energy. The 15.2 cm deep CsI crystal can stop a 260 MeV proton while a NaI crystal would need to be 19.05 cm deep to stop the same 260 MeV proton. CsI crystals have a longer decay constant than NaI crystals (1100 versus 230 ns). This is normally a disadvantage at high

counting rates because pileup may occur. However, in this experiment pileup pulses were relatively infrequent, as the Pb and $CH_2$ attenuators placed in the beamline greatly reduced the number of low energy gamma rays and neutrons in the beam. The high voltage on each CsI detector was set so that the output signals for a given charged particle were approximately equal. As the energy of the detected particle increases, there is increasingly greater probability that the particle will undergo a nuclear interaction within the CsI crystal and therefore the full energy of the proton will not be detected. This effect varies from about a 4% loss of full energy output at 60 MeV to about a 22% loss at 200 MeV and is taken into account in the detector efficiency calculations described later. Calculations from Ref. [31] were used for the CsI(Tl) nuclear interaction losses.

### I. Live converters

A converter is required to detect the scattered neutrons by converting them into charged particles (protons). An efficient way to do this is with a $CH_2$ converter via the $H(n,p)$ interaction. The original $(n,n)$ detector telescope used at CNL/UC Davis used a thin sheet of $CH_2$ as the converter. Since energy deposited in the converter by the recoil proton could not be measured, it had to be assumed that the interaction took place half way through. Thus the energy loss calculation was inaccurate. Therefore the converter had to be relatively thin to minimize the degradation to the energy resolution This was not a problem at CNL as the high monoenergetic neutron flux ($3.2\times10^6$ neutrons/s at the experimental target) provided adequate counting rate with a thin converter. However at LANSCE the neutron flux in any given energy bin in the continuum beam (about $1.0\times10^3$ neutrons/s/bin) is much smaller than the CNL neutron flux. Therefore, a thin inactive plastic converter such as that used at CNL, was impractical due to the low data rate. A solution to this problem was to use a scintillating hydrogenous converter which could be thicker to increase data rate, and also could provide a measure of the energy loss of the recoil proton within the converter. The light collection efficiency was mapped as function of position.

To measure the energy of the scattered neutron, it is necessary to determine if the neutron interacted with the H or the C in the converter. The $H(n,p)$ $Q$ value is 0.0 MeV while the $C(n,p)$ $Q$ value is −12.6 MeV so a kinematic separation is possible if the conversion scattering angle is limited to angles smaller than some value, typically near 10° in this experiment. Since $H(n,p)$ cross sections are well known, it was decided to use only this reaction and to eliminate as well as possible $C(n,p)$ conversion events. This decision means that a high H/C ratio in the converter is preferable. Since typical plastic scintillating materials have a H/C=1.1, the feasibility of using a liquid scintillator with a H/C=1.9 was also investigated. However, for simplicity, the plastic was chosen.

To test the feasibility of using an active converter, experiments were performed at CNL using 6 and 10 mm thick large area (30 cm×30 cm) plastic scintillators [24]. These tests showed that the use of an active converter increased the event rate without appreciably degrading the energy resolution. Based on these results, 30 cm×60 cm BC-401 converters were used in the WNR experiment. LC1 was 20 mm thick and LC2 was 10 mm thick. Both converters use fishtail light pipes to connect the scintillator to the photomultiplier tube.

### J. Fission chamber

The fission chamber [32], placed downstream from the target, was used to measure the beam flux. The fission chamber had an active 6.65 cm radius and so sampled the total beam flux. It used a thin foil consisting of 678 $\mu g/cm^2$ of $^{238}U$ deposited on a backing of 127 $\mu$m of stainless steel. Beam neutrons interacting with the $^{238}U$ can cause a fission event. That event is detected and the flux at each neutron energy (given by TOF) is calculated by knowing the fission cross sections of $^{238}U$ and the efficiency of detecting the fission. For each target the number of events correlated well with the integrated proton beam.

### K. Angular resolution

The angular resolution is determined by how well the spatial positions of the target $(n,n)$ scattering and the $H(n,p)$ conversion points can be determined. There is also a functional dependence on the distance between the two points and the actual scattering angle. Since the entire target is immersed in the neutron beam the scattering point could be anywhere within the target. Thus the uncertainty in the $x$ and $y$ positions of that point is about 2 cm while the absolute uncertainty in the $z$ (beam direction) coordinate is about 2 cm. The conversion point of the event within the live converters is localized in the $z$ direction by determining in which LC the conversion occurred. The $x$ and $y$ coordinates of the conversion point are determined by the trace back of the straight-line flight path determined by the hit points measured on DC3 and DC4. The drift chambers have a position resolution of 125 $\mu$m [26]. This gives a negligible $x$ and $y$ uncertainties of the conversion point when compared to the scattering point. An estimate of the angular resolution $\sigma_\theta$ due to the finite size of the target and a distance of 110 cm to the conversion point gives $\sigma_\theta \approx 0.9°$ for $\theta=15°$. A Monte Carlo (MC) calculation was performed to obtain a better estimate of the angular resolution. The MC calculation used neutrons that originated randomly throughout the target and measured the distribution of angles formed when a neutron passed through a 1 mm square section of the center of LC1. This distribution had a Gaussian $\sigma_\theta=0.80°$. Multiple Coulomb scattering of protons contributes a few percent for a resultant $\sigma_\theta=0.82°$. This value is used in the following sections.

### L. Energy resolution

Because the neutron beam has a continuum of energies, there is only a very small neutron flux at a given neutron energy. It is necessary to sum over a range of incident neutron energies to achieve sufficient statistics. Here we are only interested in elastic scattering where the excitation energy $E_{exc}=0$. The predicted energy resolution of the system for

TABLE II. Components of expected energy resolution, in MeV.

| Source of energy uncertainty | rms resolution at 65 MeV | rms resolution at 200 MeV |
|---|---|---|
| $\sigma_{\mathrm{CsI}}$ | 0.32 | 0.55 |
| $\sigma_{LC}$ | 0.25 | 0.38 |
| $\sigma_{straggling}$ | 0.29 | 0.27 |
| $\sigma_{E_{inc}}$ | 0.10 | 0.51 |
| $\sigma_{\theta}$ | 0.26 | 0.78 |
| Total resolution $\Delta E$ (FWHM) | 1.4 | 2.8 |

$E_{exc}$ is used to determine the range of $E_{exc}$ values accepted for the elastic peak. Table II gives the energy resolutions of the components that contribute. The largest contribution comes from the uncertainty in the kinetic energy of the recoil proton, $E_p$, through the uncertainties in the CsI detector, the LC, and the straggling; viz., $\sigma^2_{E_p}=\sigma^2_{\mathrm{CsI}}+\sigma^2_{straggling}+\sigma^2_{LC}$. The uncertainties in $E_p$ and $E_{exc}$ are also dependent on the angular resolution $\sigma_{\theta}$, as shown in Table II. The uncertainty $\sigma_{E_{inc}}$ in $E_{inc}$ is dependent upon the timing resolution of the $\Delta E$ detector since the incident neutron energy is determined by time of flight. The timing resolution determined from the width of the gamma rays peak was found to average 1.16 ns (see next section). This is a bit larger than predicted from the 0.75 ns resolution of $\Delta E$, the 230 ps average width of the proton beam, which is tuning and temperature dependent (due to the long duration of the runs and possible elongation of the cable carrying the micropulse timing signal $T_o$ from the accelerator, since it was exposed to the sun), and target length effects. $\sigma_{E_{inc}}$ increases as $E_{inc}$ increases since the time of flight decreases, and the time interval between separate energies decreases.

The values for $\sigma_{\mathrm{CsI}}$ were taken as given by Sorenson [26], since the same CsI(Tl) detectors were used in both experiments. The two major contributions to $dE/dx$ energy losses are from the $\Delta E$ detector (0.60 g/cm$^2$ $CH_{1.1}$) and from the front plate of the $E$ detector (0.22 g/cm$^2$ Al). The drift chambers and the air between detectors are included in the energy loss calculations but have a negligible effect on $\sigma_{straggling}$. Mean values for $\sigma_{LC}$ (averaged over all conversion points) were calculated by the method described in Ref. [24]. The 65 MeV value for $\sigma_{LC}$ assumes that the $n$-to-$p$ conversion occurs only in LC2 while the 200 MeV value assumes that the $n$-to-$p$ conversion occurs in either LC.

Table II shows the major contributors to the predicted energy resolution at 65 and 200 MeV. All values are in MeV. The various $\sigma$'s are the Gaussian rms $\sigma$, while the total resolution is FWHM. The five $\sigma$'s are added in quadrature and multiplied by 2.35 to achieve the total (FWHM) resolution. The combined effects of $\sigma_{\mathrm{CsI}}$, $\sigma_{straggling}$, and $\sigma_{\theta}$ were measured using the thin $CH_2$ target calibration runs for the CsI detector with both LC1 and LC2 removed from the detector telescope. For all energies summed together in $(n,p)$ mode this resolution was 2.2 MeV.

The special calibration runs for LC1 and LC2 can also be used to obtain a measure of the resolution of each LC independently. This was accomplished by measuring the total resolution with each converter in place and comparing to the total $(n,p)$ resolution with neither converter in place. For LC1 the total resolution is 2.4 MeV FWHM (see Fig. 2) which gives a $\sigma'_{LC1}$ of 0.41 MeV flux weighted over all energies and LC2 had a 2.6 MeV FWHM over all incident energies, which leads to $\sigma'_{LC2}=0.59$ MeV. These values are larger than the $\sigma_{LC}$ above because for each event the proton passed through the total thickness of the LC and in addition are flux weighted.

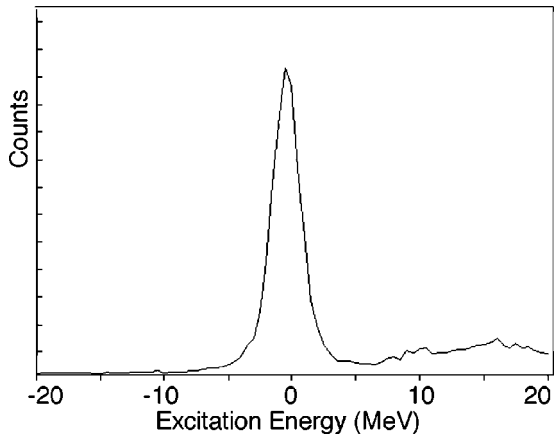


FIG. 2. Excitation energy spectrum for thin $CH_2(n,p)$ assuming $n$-H kinematics for all incident neutron energies with LC2 removed from detector telescope.

The resolution (FWHM) in excitation energy achieved for the $^{12}C(n,n)$ runs varies from 2.5 MeV for $60<E_{inc}<70$ MeV at $8<\theta_{nn}(\mathrm{lab})<10°$ to 4.5 MeV for $80<E_{inc}<90$ MeV at $14<\theta_{nn}(\mathrm{lab})<16°$ and average about 3.7 MeV [see Fig. 3(a)]. For $Ca(n,n)$ and $Pb(n,n)$ [Figs. 4(a) and 5(a)] resolutions vary from 4.0 MeV for $60<E_{inc}<70$ MeV at $8<\theta_{nn}(\mathrm{lab})<10°$ to about 6.1 MeV for $200<E_{inc}<250$ MeV at $8<\theta_{nn}(\mathrm{lab})<10°$ with an average of about 4.5 MeV. In general, the measured energy resolutions are worse than the expected values (Table II). Some of the differences are likely due to the effects of background subtraction, which are not included in the Table II estimates. Also, count rate or long term photomultiplier tube gain shifts (typically 1–2 % per day) worsen resolution.

### M. Trigger

Four triggers were used in this experiment. These triggers were the main $(n,n)$ trigger, the prescaled $(n,p)$ trigger, the fission chamber trigger, and the cosmic ray trigger. The main $(n,n)$ trigger required coincidences between $E$, $\Delta E$, LC, $T_o$, and $\overline{V}$. $E$ is a signal from at least one of the $E$ detectors, $\Delta E$ is a signal from the $\Delta E$ detector, LC is a signal from either LC1 or LC2, $T_o$ is a signal from the accelerator that indicated the presence of a micropulse and also served as a stop signal for the time of flight, and $\overline{V}$ is the absence of a signal from the veto paddle. The prescaled $(n,p)$ trigger was a coincidence between $E$, $\Delta E$, and $T_o$. This trigger was sent through

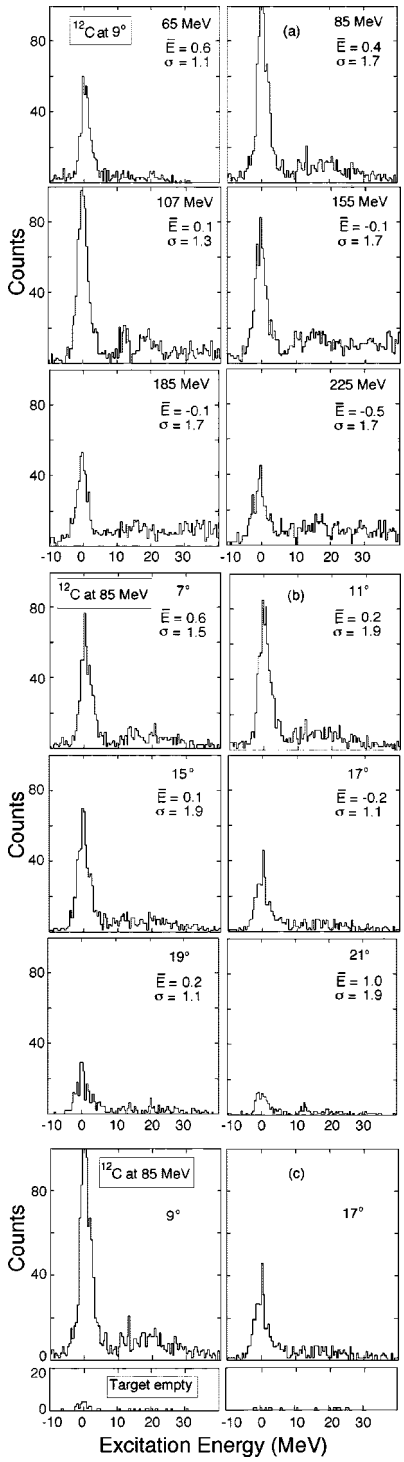


FIG. 3. (a) $^{12}$C$(n,n)$ excitation energy spectra for $8<\theta_{nn}<10°$ at various incident neutron kinetic energies. (b) $^{12}$C$(n,n)$ excitation energy spectra for $80<E_{inc}<90$ MeV at various neutron scattering angles. (c) Comparison of excitation energy histograms for $^{12}$C$(n,n)$ (upper) and for target empty (lower) with $80<E_{inc}<90$ MeV and at $8<\theta_{nn}(\text{lab})<10°$ (left) and $16<\theta_{nn}(\text{lab})<18°$ (right).

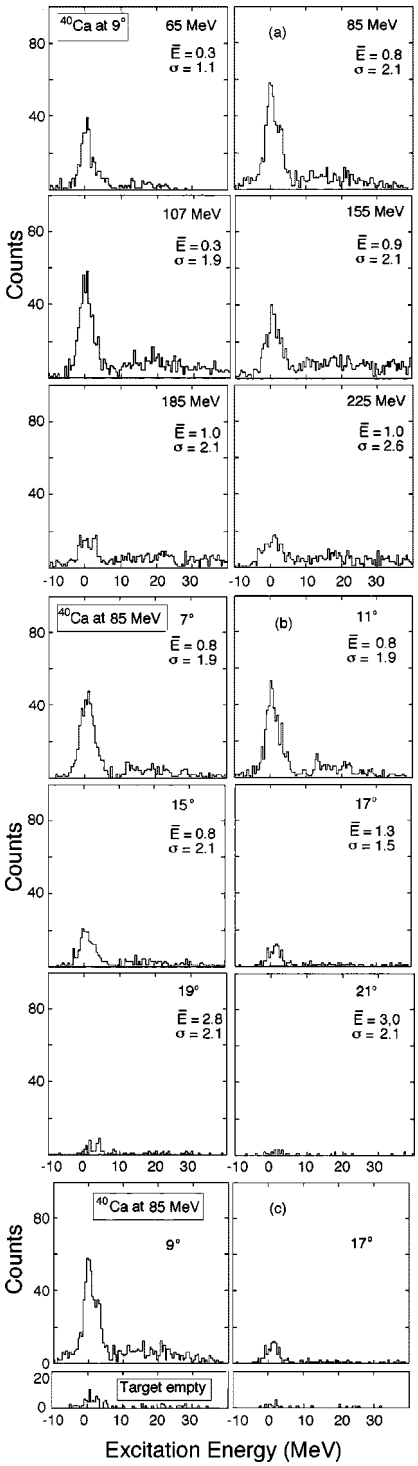


FIG. 4. (a) $^{40}$Ca$(n,n)$ excitation energy spectra for $8<\theta_{nn}<10°$ at various incident neutron kinetic energies. (b) $^{40}$Ca$(n,n)$ excitation energy spectra for $80<E_{inc}<90$ MeV at various neutron scattering angles. (c) Comparison of excitation energy histograms for $^{40}$Ca$(n,n)$ (upper) and for target empty (lower) with $80<E_{inc}<90$ MeV and at $8<\theta_{nn}(\text{lab})<10°$ (left) and $16<\theta_{nn}(\text{lab})<18°$ (right).

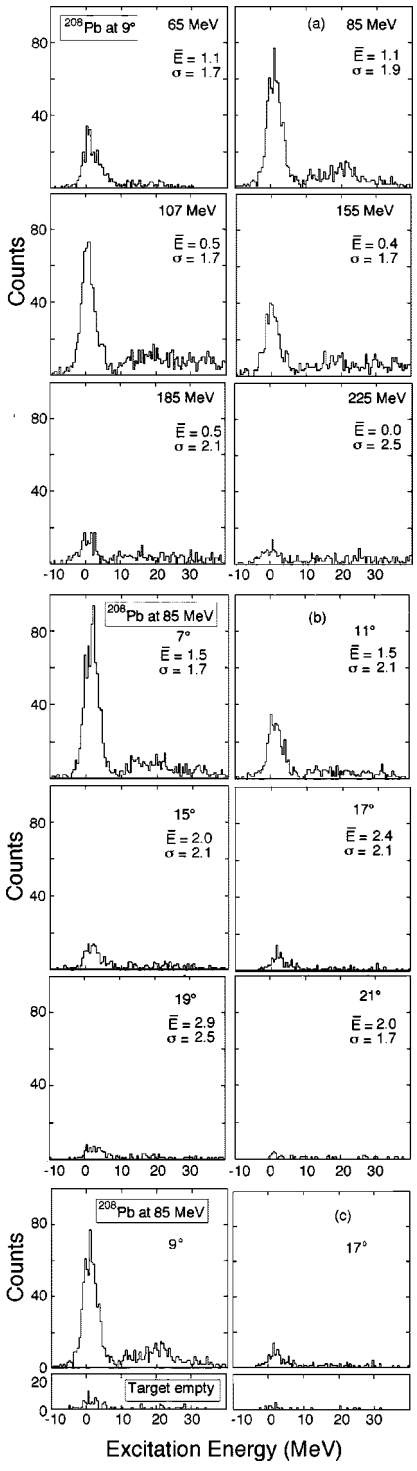


FIG. 5. (a) $^{208}$Pb$(n,n)$ excitation energy spectra for $8<\theta_{nn}<10°$ at various incident neutron kinetic energies. (b) $^{208}$Pb$(n,n)$ excitation energy spectra for $80<E_{inc}<90$ MeV at various neutron scattering angles. (c) Comparison of excitation energy histograms for $^{208}$Pb$(n,n)$ (upper) and for target empty (lower) with $80<E_{inc}<90$ MeV and at $8<\theta_{nn}$(lab)$<10°$ (left) and at $16<\theta_{nn}$(lab)$<18°$ (right).

TABLE III. Detector parameters for data analysis.

| |
|---|
| Kinetic energy of the incoming neutron |
| Particle identification of recoil/converted particle (protons) |
| Flight path trajectory of the recoil proton |
| Kinetic energy of recoil protons |
| Scattering angle of scattered neutrons |
| Kinetic energy of scattered neutrons |
| Excitation energy of the target nuclei |
| Neutron beam flux for normalization |

a $\times 10$ prescaler. Thus only one out of ten coincidences would be used as an $(n,p)$ event trigger. All $(n,z)$ events from both the experimental target and the TP use this trigger.

## III. DATA ANALYSIS

Data were acquired using a CAMAC-based acquisition system and a Microvax II computer using the *Q* data acquisition software developed at LANSCE. Events were written directly to a hard disk on the computer and then backed up to 8 mm video tape. The data were analyzed on the VAX 4000-90 computer cluster of the Nuclear Physics Group at UC Davis. To characterize the $(n,n)$ elastic events with this detector system the parameters were determined as in Table III.

The kinetic energy of the incident neutron projectile is measured via time of flight. The time difference between the reference gamma ray peak (FWHM 1.16 ns, mainly from the neutron production target) and the current event is used along with the total flight path length from the center of the neutron production target to the $\Delta E$ detector to calculate the neutron energy. This difference reduces some of the uncertainties, such as those due to $\Delta E$ detector response. A typical neutron time-of-flight spectrum is shown in Fig. 6(a), and the derived neutron kinetic energy spectrum is shown in Fig. 6(b).

Data were taken in two runs a year apart. The data were binned in 10 MeV bins from 60 to 100 MeV and larger bins above 100 MeV as given in Table IV. The neutron scattering angle bins are 2° everywhere.

The recoil particle is identified by plotting energy loss from $\Delta E$ versus energy for each of the 15 CsI detectors and placing hyperbolic cut curves around the band of points that are due to protons. The proton flight path is determined by the two spatial points given by the hit positions on DC3 and DC4. Since there is no significant magnetic field present, the flight path of the proton can be approximated by a straight line through the hit positions on DC3 and DC4 from the live converters to the *E* detector. The straight-line flight path is used to calculate the $dE/dx$ energy losses of the recoil proton between LC2 and the *E* detector. The flight path is also used, in conjunction with the scattered neutron flight path from target to converter, to calculate the conversion/recoil angle of the proton. This angle is used in the calculation of scattered neutron energy and in the minimization of the number of

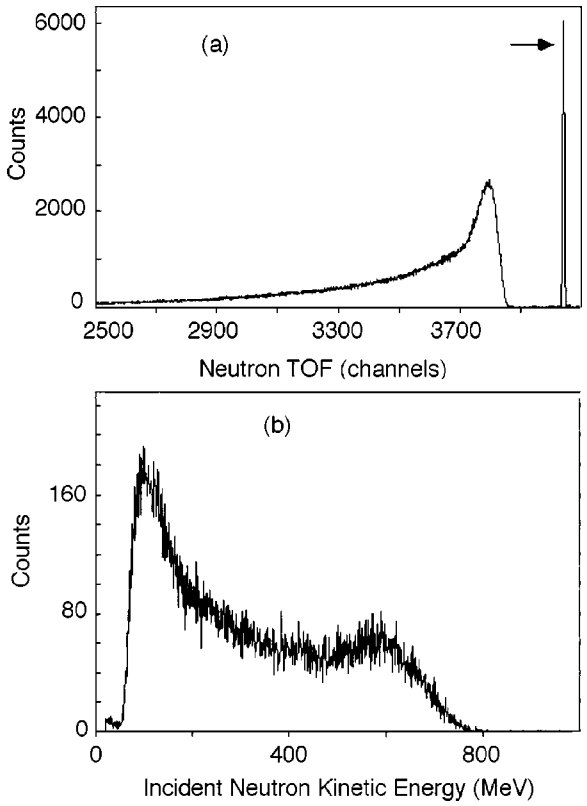


FIG. 6. (a) Neutron time-of-flight spectrum. The arrow points to the gamma ray peak. (b) Kinetic energy spectrum of the incident neutron, $E_{inc}$.

events analyzed that are due to protons produced by the $^{12}C(n,p)$ reaction in the live converter.

The kinetic energy of the recoil proton is calculated via $E_p = E_{CsI} + E_{loss} + E_{LC2} + E_{LC1}$ where $E_{CsI}$ is the measured energy deposited in the $E$ detector; $E_{loss}$ is the calculated energy lost by the proton between LC2 and $E$; and $E_{LC2}$ and $E_{LC1}$ are the measured energies deposited in LC2 and LC1, respectively.

The kinetic energy of the scattered neutron is calculated using the recoil proton energy and angle. By limiting the $(n,p)$ conversion angle to be less than or equal to 10°, the protons produced from the $^{12}C$ reactions can be reduced to a small background kinematically for incident neutron energies up to $\approx$250 MeV.

TABLE IV. Incident neutron kinetic energy bins.

| Energy—low (MeV) | Energy—high (MeV) | Mean energy (MeV) | Mean energy (flux weighted) |
|---|---|---|---|
| 60 | 70 | 65.0 | 64.9 |
| 70 | 80 | 75.0 | 74.9 |
| 80 | 90 | 85.0 | 84.9 |
| 90 | 100 | 95.0 | 94.9 |
| 100 | 115 | 107.5 | 107.4 |
| 115 | 140 | 127.5 | 127.2 |
| 140 | 170 | 155.0 | 154.5 |
| 170 | 200 | 185.0 | 184.4 |
| 200 | 250 | 225.0 | 223.2 |

The neutron scattering angle is calculated by first finding the $(x,y)$ hit point of the recoil proton on either LC1 or LC2 depending on where the proton originated. The $z$ coordinate is determined by whether the proton originated in LC1 or LC2 and is chosen to be at the center of that converter. The flight path of the scattered neutron is assumed to be a straight line between the center of the experimental target at $(x,y,z)=(0,0,0)$ and the converter hit point. The neutron scattering angle is the angle between the neutron flight path and the neutron beam.

The last piece of information needed to characterize an event is the determination of whether the event is an elastic scattering event. This is determined by calculating the center of mass excitation energy $E_{exc}$, which for an elastic scattering event should equal zero. To allow for finite energy resolution of the system, the NN92 acceptance used was $-5.0 < E_{exc} < 5.0$ MeV while NN93 runs used $-4.0 < E_{exc} < 6.0$ MeV. The reason for the difference was a gain shift between data and calibration runs for NN93. (NN refers to neutron elastic scattering. The numbers refer to the year of the data taking.)

### A. Background subtraction

The target empty data were normalized to the target data using the total number of beam micropulses ($T_o$'s). This normalization would normally be done using the integrated number of neutrons from the neutron monitor. However, the monitor failed during a number of background runs. For normalization to number of beam pulses to be valid the number of protons per micropulse and the neutron spectrum shape should not vary significantly. This was verified to ±10% by comparing runs where the monitor was available, and monitoring the ratio of target-in events to $T_o$'s for different incident energy bins. The empty events were a small fraction (a few percent) of target data except for a few larger angles where up to 6% was measured. So the 10% normalization uncertainties had a negligible effect on those of the final data.

Although kinematic cuts were made to exclude protons from the $^{12}C(n,px)$ reaction in the converters, the finite resolution of the system allowed some of these into the data, especially at higher neutron beam energies. The size of this background was estimated by summing the counts in 3 MeV bins immediately to the left and right of the elastic scattering peak in the excitation energy spectrum. At 85 MeV this effect varied from 4% at low angles to 20% at the large angles. At 155 MeV this effect ranged from 8% to 30%, while at 225 MeV the effect varied from 12% to 50%. The associated systematic uncertainty is discussed in the next section.

### B. Cross section calculations

Figure 7 shows the average beam flux measured by the fission chamber for NN93 runs, and binned in 10 MeV intervals from 40 to 260 MeV incident neutron kinetic energy. For these runs there were approximately $1 \times 10^8$ protons per

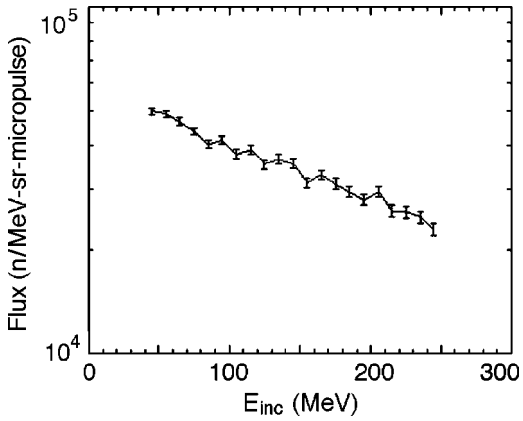


FIG. 7. Average measured neutron beam flux.

micropulse, before an accelerator modification, which now results in an increase in current to more than $6\times10^8$ protons per micropulse. At each energy the flux was measured in units of neutrons/MeV/micropulse/sr where sr corresponds to the solid angle subtended by the experimental target as seen by the white neutron source. The data from a given data set were averaged over all the runs of that data set to calculate an average value for the flux in each incident bin, as shown in Fig. 7. This was necessary because fission chamber data are not available from every individual run. The energy dependence of the flux for each run was individually compared to the energy dependence of the average flux to check for any fluctuations of the incident neutron flux over time. No statistically significant fluctuations or target-related differences were found and the average value for the flux was used. (Since the neutron monitor was downstream of the target, the measured flux could be corrected for target attenuation using tabulated total cross sections. The area-weighted beam attenuation losses calculated for each of the three targets were nearly the same; i.e., within 1% for all energies.)

The weighted average of the measured flux within the desired $E_{inc}$ bins, as given in Table IV, was then used to normalize the neutron counts to the incident neutron flux for each energy bin. The effect of neutron beam polarization (see above in Sec. II A) was calculated to be less than 10% of the combined statistical and systematic uncertainties, and no corrections for polarization were made.

The absolute efficiency $F$ of the detector system was obtained using a Monte Carlo calculation [33]. This is discussed in Appendix A. This efficiency uses *n-p* cross section parametrizations and includes both the geometric acceptance of the detector telescope and the conversion efficiency of the live converters. The solid angle and efficiency are 7 msr and 0.05%, respectively, at 150 MeV and 16°, for example. Corrections for attenuation and multiple scattering of the beam and scattered flux into the detector were also estimated and included in the systematic uncertainties. See Appendix A.

With the efficiency ($F$) and flux ($I$) determined, it is possible to calculate $d\sigma/d\Omega$ using Eq. (A1) in Appendix A. The final calculation is to convert the laboratory angles and cross sections to center-of-mass angles and cross sections. Relativistic kinematics and Jacobians are used in this conversion.

## IV. RESULTS

The measured elastic scattering differential cross sections for $^{12}$C, $^{40}$Ca, and $^{208}$Pb are presented. A major source of uncertainty in these experiments is statistical due to the relatively low number of counts in each energy bin for both target-in and background runs. For $^{12}C(n,n)$ these errors (one standard deviation uncertainties) varied between 4.3% and 13.4% for angles up to 18.7° and from 7.7% to 30.4% at higher angles with one bin at 93%. For the $^{40}Ca(n,n)$ data the statistical errors varied between 5% and 105% with the large angles at high energy bins having the largest errors. The $^{208}Pb(n,n)$ data statistical errors varied between 4% and 80% with seven large angle bins greater than 100%.

The statistical error in the flux measurement was approximately 3% while the statistical error in the efficiency calculation was less than 2%. The three statistical errors were added in quadrature to calculate the overall statistical error tabulated with the differential cross sections in Tables V–X (see Appendix B).

There are several significant systematic errors. One of these is due to imprecise measurement of the detector geometry. This mainly affects the accuracy of the efficiency calculation. The efficiency Monte Carlo is very sensitive to edge effects in the geometry, particularly at small angles where the edge of the $E$ detector places a lower limit on the scattering angle. A systematic error of 20% has been assigned to the 6°–8° laboratory scattering angle bin due to this edge effect. Also, due to the uncertainties of the parametrizations used for the $H(n,p)$ cross sections (see Appendix A) used in the efficiency MC calculation, an overall systematic error of 5% has been assigned for all energies. In addition, the uncertainties in corrections for angular resolution and multiple scattering effects (Appendix A) increased the systematic uncertainties at and near cross section minima; i.e., for Pb and for Ca at the highest three energies.

Another source of systematic error is contamination from C conversions discussed earlier. This contamination should only be significant at the highest energies due to the degradation of the resolution of excitation energy at 200 MeV (see Table II). This effect was estimated by looking at the number of counts in the excitation energy spectrum in the 3 MeV bins to the left and to the right of the peak gate and used to correct the counts in the elastic peak. The total counts in these two bins were compared to the counts in the elastic peak and the percentage of the counts in the elastic peak was used to estimate the associated systematic error.

Another possible systematic error is due to the population of low excited states in the target nuclei. This was checked using the computer code of Kunz, DWUCK4 [34], to calculate angular distributions for the $(p,p')$ reaction and the $(n,n')$ reaction to a specific excited state. The $(p,p')$ distributions were compared to experimental $(p,p')$ cross sections to determine the normalization factor needed to convert the DWUCK4 output for the $(n,n')$ distributions for the same target to differential cross section predictions for the excited states.

For $^{12}C(n,n')$ only the 4.44 MeV $2^+$ state is close enough in energy to affect the elastic peak. The DWUCK4 predictions

TABLE V. Cross section for $^{12}C(n,n)$.

| Energy (MeV) | Angle (deg) (c.m.) | $d\sigma/d\Omega$ (mb/sr) | ± (statistics) (mb/sr) | ± (systematic) (mb/sr) |
|---|---|---|---|---|
| 65 | 7.6 | 1113 | 88 | 265 |
| | 9.8 | 1088 | 76 | 67 |
| | 12.0 | 909 | 67 | 56 |
| | 14.2 | 822 | 58 | 41 |
| | 18.5 | 574 | 53 | 29 |
| | 20.7 | 491 | 47 | 28 |
| | 22.8 | 277 | 46 | 20 |
| 75 | 7.6 | 1038 | 91 | 257 |
| | 9.8 | 1112 | 84 | 56 |
| | 12.0 | 894 | 72 | 54 |
| | 14.2 | 795 | 65 | 58 |
| | 18.5 | 510 | 50 | 28 |
| | 20.7 | 395 | 40 | 25 |
| | 22.9 | 323 | 46 | 22 |
| 85 | 7.6 | 915 | 60 | 241 |
| | 9.8 | 1028 | 57 | 58 |
| | 12.0 | 829 | 48 | 67 |
| | 14.2 | 586 | 39 | 54 |
| | 18.5 | 397 | 30 | 26 |
| | 20.7 | 266 | 26 | 14 |
| | 22.9 | 191 | 24 | 14 |
| 95 | 7.6 | 861 | 62 | 230 |
| | 9.8 | 1011 | 55 | 68 |
| | 12.0 | 806 | 49 | 68 |
| | 14.2 | 632 | 41 | 59 |
| | 18.5 | 398 | 28 | 26 |
| | 20.7 | 305 | 25 | 31 |
| | 22.9 | 171 | 21 | 18 |
| 107.5 | 7.6 | 962 | 57 | 266 |
| | 9.8 | 943 | 50 | 89 |
| | 12.0 | 666 | 39 | 81 |
| | 14.2 | 538 | 35 | 63 |
| | 18.6 | 313 | 23 | 25 |
| | 20.7 | 234 | 21 | 27 |
| | 22.9 | 136 | 16 | 17 |

TABLE VI. Cross section for $^{12}C(n,n)$ (continued).

| Energy (MeV) | Angle (deg) (c.m.) | $d\sigma/d\Omega$ (mb/sr) | ± (statistics) (mb/sr) | ± (systematic) (mb/sr) |
|---|---|---|---|---|
| 127.5 | 7.7 | 772 | 45 | 233 |
| | 9.8 | 694 | 39 | 89 |
| | 12.0 | 590 | 32 | 66 |
| | 14.2 | 400 | 24 | 64 |
| | 18.6 | 178 | 16 | 28 |
| | 20.8 | 116 | 14 | 16 |
| | 22.9 | 86 | 15 | 13 |
| 155 | 7.7 | 642 | 43 | 198 |
| | 9.9 | 617 | 35 | 90 |
| | 12.1 | 417 | 29 | 60 |
| | 14.2 | 294 | 21 | 53 |
| | 18.6 | 119 | 16 | 24 |
| | 20.8 | 92 | 11 | 15 |
| | 23.0 | 41 | 12 | 8.1 |
| 185 | 7.7 | 620 | 44 | 193 |
| | 9.9 | 553 | 34 | 67 |
| | 12.1 | 335 | 26 | 47 |
| | 14.3 | 213 | 22 | 41 |
| | 18.7 | 90 | 12 | 24 |
| | 20.8 | 61.3 | 9.3 | 17 |
| | 23.0 | 50.4 | 9.8 | 12 |
| 225 | 7.7 | 478 | 40 | 169 |
| | 9.9 | 416 | 29 | 73 |
| | 12.1 | 232 | 22 | 51 |
| | 14.3 | 170 | 17 | 34 |
| | 18.7 | 77.7 | 9.5 | 30 |
| | 20.9 | 32.7 | 10.0 | 11 |
| | 23.1 | 10.4 | 9.7 | 4.3 |

were compared with $(p,p')$ data [35] at 65 MeV and also data [36] at 155 MeV. These comparisons showed that DWUCK4 predictions needed a 0.35 normalization factor. This factor was applied to the DWUCK4 predictions for $(n,n')$. The cross section due to the 4.44 MeV $2^+$ state has less than a 1% effect on the measured elastic cross section at all angles less than 18° (c.m.). At 18.5° (c.m.) the effect varies from 1.2% at 75 MeV to 2.8% at 225 MeV. For data from the 20.8° (c.m.) bin the effect varies from 1.5% to 5.3% while for the bin at the largest angle (22.8°) the effect varies from 1.8% to 11.7%.

The results of a $^{40}Ca(p,p')$ experiment [37] at 65 MeV show three excited states that could effect the elastic scattering data. These states are 3.73 MeV $3^-$ state, a 3.90 MeV $2^+$ state, and a 4.48 MeV $5^-$ state. The inelastic data was compared to 65 MeV predictions from DWUCK4 and a normalization factor for the DWUCK4 output of 0.075 was calculated. The only excited state that has a significant effect is the 3.73 MeV $3^-$ state. The largest effect was 39.5% at 21.6° (c.m.) for 127.5 MeV neutrons. There are six energy bins with about a 15% effect with remaining bins varying from $<1\%$ to 11%.

There are two excited states of $^{208}$Pb, 2.61 MeV $(3^-)$ and 3.20 MeV $(5^-)$ [38], that could underlie the elastic peak. Comparison of the DWUCK4 predictions for the 2.61 MeV $3^-$ state with $(p,p')$ data [38] gives a normalization factor for the DWUCK4 output of 0.0036. The DWUCK4 predictions for the $(n,n')$ cross sections indicate only a few bins have a greater than 1% effect while only one bin (155 MeV, 19.1°) has an effect greater than 3.5%. That bin has 36.7% of its counts attributed to the 2.61 MeV $3^-$ state. The possible inclusion of excited states in the elastic peak is treated as a systematic error and is included in the tabulated cross sections with the other systematic errors.

TABLE VII. Cross section for $^{40}$Ca$(n,n)$.

| Energy (MeV) | Angle (deg) (c.m.) | $d\sigma/d\Omega$ (mb/sr) | ± (statistics) (mb/sr) | ± (systematic) (mb/sr) |
|---|---|---|---|---|
| 65 | 7.2 | 4660 | 410 | 1090 |
| | 9.2 | 4780 | 340 | 180 |
| | 11.3 | 3940 | 310 | 180 |
| | 13.3 | 2600 | 260 | 120 |
| | 15.4 | 1890 | 210 | 110 |
| | 17.5 | 1210 | 170 | 50 |
| | 19.5 | 768 | 142 | 22 |
| | 21.6 | 537 | 127 | 38 |
| 75 | 7.2 | 4380 | 440 | 1070 |
| | 9.2 | 4970 | 380 | 270 |
| | 11.3 | 2780 | 280 | 170 |
| | 13.4 | 2620 | 260 | 150 |
| | 15.4 | 2200 | 240 | 60 |
| | 17.5 | 1130 | 170 | 70 |
| | 19.5 | 632 | 131 | 18 |
| | 21.6 | 307 | 102 | 24 |
| 85 | 7.2 | 4940 | 300 | 1100 |
| | 9.2 | 3770 | 220 | 240 |
| | 11.3 | 3140 | 200 | 170 |
| | 13.4 | 2020 | 160 | 130 |
| | 15.4 | 1450 | 130 | 90 |
| | 17.5 | 700 | 92 | 41 |
| | 19.5 | 313 | 62 | 41 |
| | 21.6 | 201 | 56 | 29 |
| 95 | 7.2 | 3780 | 270 | 900 |
| | 9.2 | 3360 | 210 | 210 |
| | 11.3 | 2650 | 180 | 170 |
| | 13.4 | 1600 | 150 | 100 |
| | 15.4 | 909 | 110 | 54 |
| | 17.5 | 407 | 68 | 56 |
| | 19.5 | 245 | 49 | 46 |
| | 21.6 | 82 | 44 | 28 |
| 107.5 | 7.2 | 3900 | 250 | 1020 |
| | 9.3 | 3280 | 190 | 250 |
| | 11.3 | 1880 | 140 | 220 |
| | 13.4 | 1430 | 120 | 130 |
| | 15.4 | 829 | 89 | 80 |
| | 17.5 | 338 | 62 | 32 |
| | 19.5 | 260 | 52 | 27 |
| | 21.6 | 105 | 35 | 27 |

TABLE VIII. Cross section for $^{40}$Ca$(n,n)$ (continued).

| Energy (MeV) | Angle (deg) (c.m.) | $d\sigma/d\Omega$ (mb/sr) | ± (statistics) (mb/sr) | ± (systematic) (mb/sr) |
|---|---|---|---|---|
| 127.5 | 7.2 | 2840 | 180 | 810 |
| | 9.3 | 2130 | 130 | 230 |
| | 11.3 | 1400 | 100 | 130 |
| | 13.4 | 712 | 74 | 97 |
| | 15.4 | 484 | 58 | 59 |
| | 17.5 | 149 | 36 | 26 |
| | 19.5 | 110 | 28 | 27 |
| | 21.6 | 25 | 18 | 16 |
| 155 | 7.2 | 1920 | 140 | 570 |
| | 9.3 | 1410 | 110 | 190 |
| | 11.3 | 877 | 81 | 101 |
| | 13.4 | 471 | 57 | 81 |
| | 15.4 | 198 | 41 | 39 |
| | 17.5 | 67 | 26 | 22 |
| | 19.5 | 55 | 25 | 16 |
| | 21.6 | 40 | 16 | 11 |
| 185 | 7.2 | 1520 | 140 | 430 |
| | 9.3 | 1040 | 95 | 170 |
| | 11.3 | 469 | 65 | 92 |
| | 13.4 | 236 | 50 | 60 |
| | 15.4 | 110 | 34 | 14 |
| | 17.5 | 56 | 23 | 17 |
| | 19.6 | 59 | 24 | 26 |
| | 21.6 | 16 | 17 | 6.1 |
| 225 | 7.2 | 942 | 105 | 290 |
| | 9.3 | 796 | 75 | 108 |
| | 11.3 | 270 | 47 | 53 |
| | 13.4 | 121 | 31 | 34 |
| | 15.5 | 91 | 24 | 21 |
| | 17.5 | 26 | 14 | 8.0 |
| | 19.6 | 18 | 11 | 4.7 |
| | 21.6 | 18 | 14 | 3.3 |

### A. $^{12}$C$(n,n)$

Various $^{12}$C$(n,n)$ excitation energy spectra given in Fig. 3 show how the spectra change with incident neutron energy. The neutron scattering angle bin remains the same while the incident energy bin is varied. $\overline{E}$ is the mean of the elastic peak while $\sigma$ is the FWHM of the elastic peak divided by 2.35. The 65 MeV spectrum shows data from neutron-to-proton conversions in LC2 only. The other five spectra are data from conversions in both LCs. All of the spectra in Fig. 3(b) have the same energy bin of $80 < E_{inc} < 90$ MeV. The figure shows how the elastic peak changes as the neutron scattering angle is increased. Typical target empty spectra are compared to the target spectrum in Fig. 3(c).

As noted earlier, the counts in the elastic peak for each $E_{inc}$ bin were corrected for target out and C$(n,px)$ events and a cross section calculated as described in Appendix A.

The calculated differential cross sections for the $^{12}$C$(n,n)$ reaction are tabulated with their estimated statistical and systematic errors in Tables V and VI (Appendix B). The data points for $14 < \theta_{nn}(\text{lab}) < 16°$ for all energies were eliminated due to a hardware problem with DC3 that mainly affected that area in space.

The first test of the cross section data was to compare the results to the previously published 65 MeV data from CNL

TABLE IX. Cross section for $^{208}$Pb$(n,n)$.

| Energy (MeV) | Angle (deg) (c.m.) | $d\sigma/d\Omega$ (mb/sr) | ± (statistics) (mb/sr) | ± (systematic) (mb/sr) |
|---|---|---|---|---|
| 65 | 7.0 | 12800 | 1070 | 2940 |
| | 9.0 | 8820 | 750 | 440 |
| | 11.1 | 3290 | 550 | 160 |
| | 13.1 | 404 | 451 | 20 |
| | 15.1 | 794 | 338 | 63 |
| | 17.1 | 910 | 316 | 91 |
| | 19.1 | 438 | 278 | 44 |
| | 21.1 | 875 | 276 | 126 |
| 75 | 7.0 | 14800 | 1270 | 3340 |
| | 9.0 | 8520 | 820 | 430 |
| | 11.1 | 4810 | 650 | 240 |
| | 13.1 | 2240 | 480 | 110 |
| | 15.1 | 1380 | 400 | 70 |
| | 17.1 | 905 | 319 | 45 |
| | 19.1 | 1380 | 320 | 75 |
| | 21.1 | 881 | 269 | 88 |
| 85 | 7.0 | 17300 | 900 | 3950 |
| | 9.0 | 9570 | 570 | 480 |
| | 11.1 | 3560 | 390 | 190 |
| | 13.1 | 1070 | 280 | 90 |
| | 15.1 | 1270 | 230 | 70 |
| | 17.1 | 1000 | 210 | 50 |
| | 19.1 | 928 | 173 | 54 |
| | 21.1 | 287 | 129 | 50 |
| 95 | 7.0 | 16100 | 900 | 3870 |
| | 9.0 | 8840 | 550 | 500 |
| | 11.1 | 3480 | 370 | 350 |
| | 13.1 | 582 | 296 | 29 |
| | 15.1 | 733 | 247 | 61 |
| | 17.1 | 1450 | 197 | 72 |
| | 19.1 | 951 | 142 | 62 |
| | 21.1 | 156 | 123 | 10 |
| 107.5 | 7.0 | 14900 | 780 | 3640 |
| | 9.0 | 8060 | 490 | 430 |
| | 11.1 | 2290 | 300 | 190 |
| | 13.1 | 925 | 212 | 90 |
| | 15.1 | 792 | 178 | 57 |
| | 17.1 | 719 | 164 | 57 |
| | 19.1 | 559 | 135 | 70 |
| | 21.1 | 281 | 89 | 32 |

TABLE X. Cross section for $^{208}$Pb$(n,n)$ (continued).

| Energy (MeV) | Angle (deg) (c.m.) | $d\sigma/d\Omega$ (mb/sr) | ± (statistics) (mb/sr) | ± (systematic) (mb/sr) |
|---|---|---|---|---|
| 127.5 | 7.0 | 12100 | 590 | 3110 |
| | 9.0 | 5100 | 320 | 550 |
| | 11.1 | 994 | 196 | 112 |
| | 13.1 | 415 | 164 | 42 |
| | 15.1 | 456 | 126 | 57 |
| | 17.1 | 507 | 108 | 56 |
| | 19.1 | 257 | 77 | 46 |
| | 21.1 | 190 | 69 | 39 |
| 155 | 7.0 | 8050 | 460 | 2110 |
| | 9.1 | 2680 | 260 | 230 |
| | 11.1 | 492 | 159 | 83 |
| | 13.1 | 531 | 127 | 49 |
| | 15.1 | 321 | 107 | 40 |
| | 17.1 | 140 | 76 | 32 |
| | 19.1 | 3.3 | 64 | 2.0 |
| | 21.1 | 97 | 37 | 11 |
| 185 | 7.0 | 4450 | 390 | 1260 |
| | 9.1 | 1410 | 200 | 210 |
| | 11.1 | 234 | 139 | 44 |
| | 13.1 | 235 | 126 | 31 |
| | 15.1 | 135 | 86 | 33 |
| | 17.1 | 26 | 54 | 2.2 |
| | 19.1 | 40 | 57 | 5.1 |
| 225 | 7.0 | 2130 | 270 | 660 |
| | 9.1 | 573 | 140 | 60 |
| | 11.1 | 10 | 105 | 17 |
| | 13.1 | 214 | 85 | 43 |
| | 15.1 | 67 | 51 | 11 |
| | 17.1 | 47 | 38 | 17 |
| | 19.1 | 10 | 25 | 4.8 |

[3]. This comparison is shown in Fig. 8(a). The error bars for the present data are the combined systematic and statistical errors while the error bars for the CNL data represent only the statistical errors. Also shown are the OM predictions using the OMP parameters from Ref. [39]. In Fig. 8(b) our 95 MeV data are compared to the recent 96 MeV data from Uppsala [6,7], and to the earlier 96 MeV data of Salmon [4] which were taken with a neutron beam whose energy width was 24 MeV (FWHM). Predictions using the OMP parameters from Comfort and Karp [39] (dotted curves) and predictions using the global OMP by Koning and Delaroche [40] (solid curves) are also shown. The latter is valid for incident energies between 1 keV and 200 MeV and nuclear masses $A$ from 24 to 209.

The data from Ref. [4] tend to fall below the trend of the other data, while our larger angle data seems to be high. The authors in Ref. [7] have done a detailed study comparing their results with several OMP predictions including the global OMP by Koning and Delaroche. The authors note that in all cases the models fail to describe the data, citing surface effects not included in the models as possible reasons, as well as the fact that $^{12}$C is not a spherical nucleus.

In Fig. 9 the energy dependence of the $^{12}$C$(n,n)$ differential cross sections are compared with the Comfort and Karp OMP predictions (dotted curves) using the parameters and energy dependence cited in Ref. [39] and the predictions-(solid curves) from the OMP by Koning and Delaroche [40].

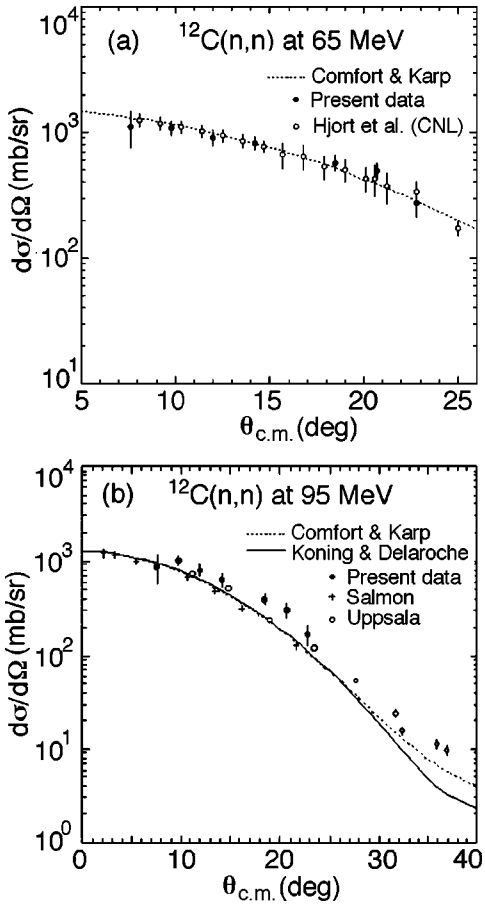


FIG. 8. (a) Comparison of $^{12}C(n,n)$ differential cross sections for $60<E_{inc}<70$ MeV from this experiment (filled circles) with the previous measurements at 65 MeV from CNL at UC Davis [3]. Also shown is the Comfort and Karp [39] OM prediction at 65 MeV. (b) Comparison of $^{12}C(n,n)$ differential cross sections for $90<E_{inc}<100$ MeV from this experiment (filled circles) with the previous measurements at 96 MeV from Salmon [4] (crosses) and Uppsala [6,7] (open circles). Also shown are the Comfort and Karp [39] and Koning and Delaroche [40] OM predictions at 95 MeV.

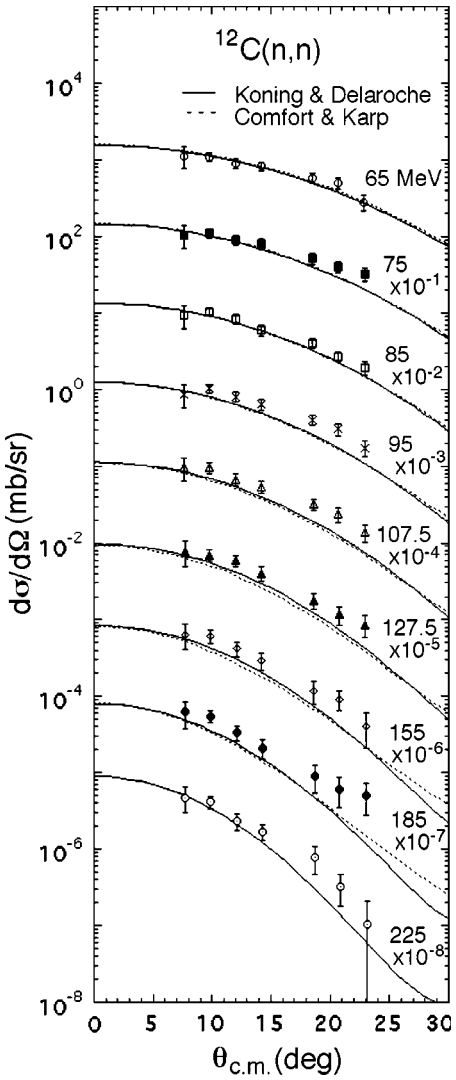


FIG. 9. Comparison of experimental data with predictions of the phenomenological OM of Comfort and Karp [39] (dotted curves) and Koning and Delaroche [40] (solid curves) for the $^{12}C(n,n)$ reaction. Please see text.

The error bars in Fig. 9 include the combined effect of the statistical errors and the systematic errors. The OMP calculations using the parameters from Ref. [39] were performed using the DWUCK4 code with the relativistic kinematics option turned on. Agreement is fair over all energies, and the two calculations agree well, bearing in mind that the model of Ref. [40] is applied outside its claimed validity region of $24<A<209$. The data are higher than the predictions at higher energies and larger angles.

The Comfort and Karp OMP was obtained by those authors by fitting proton elastic and analyzing power for C at discrete energies from 12.1 to 183 MeV (12.1, 21.6, 40, 61.4, 96, 122, 135, and 183 MeV). The predictions at the energies presented here were obtained by interpolating the parameters given in Ref. [39].

### B. $^{40}$Ca$(n,n)$

Typical excitation energy spectra for the $^{40}Ca(n,n)$ reaction are shown next. Figure 4(a) shows the behavior of the elastic peak over several energy bins as the scattering angle bin is held constant while Fig. 4(b) shows the behavior of the elastic peak over a range of angular bins while keeping the same incident neutron kinetic energy bin. Target-in and target-out spectra for one $E_{inc}$ bin and two angles are compared in Fig. 4(c). The measured differential elastic cross sections for the $^{40}Ca(n,n)$ reaction are tabulated in Tables VII and VIII (Appendix B) along with their estimated errors.

The present results for the $^{40}Ca(n,n)$ differential cross sections measured at the 65 MeV energy bin are compared with those from CNL [3] in Fig. 10(a). The CNL cross sections appear to fall off somewhat faster with angle. They do not include systematic uncertainties while the present data do. The overall agreement at all but the last angle is good. In Fig. 10(b) the measurements for the 85 MeV energy bin are compared with those for $^{40}Ca(p,p)$ at 80 MeV measured by Nadasen *et al.* [42]. Also shown are the corresponding OMP calculations using the Schwandt *et al.* OM parameters [41].

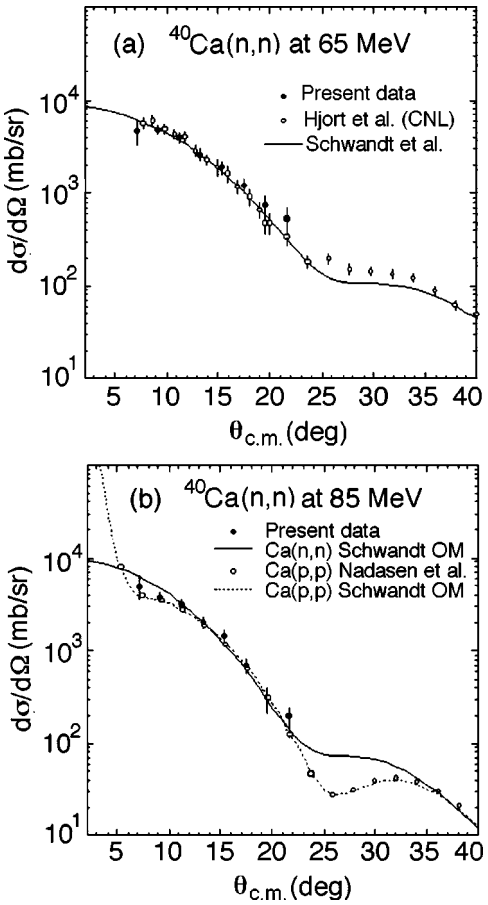


FIG. 10. (a) Comparison of $^{40}$Ca$(n,n)$ differential cross sections for $60<E_{inc}<70$ MeV from this experiment (filled circles) with the 65 MeV data taken at CNL at UC Davis [3] (open circles). Also shown is the Schwandt *et al.* [41] OM prediction at 65 MeV. (b) Comparison of $^{40}$Ca$(n,n)$ differential cross sections for $80<E_{inc}<90$ MeV from this experiment (filled circles) with those for $^{40}$Ca$(p,p)$ at 80 MeV from Nadasen *et al.* [42] (open circles). Also shown are the corresponding Schwandt *et al.* [41] OM predictions.

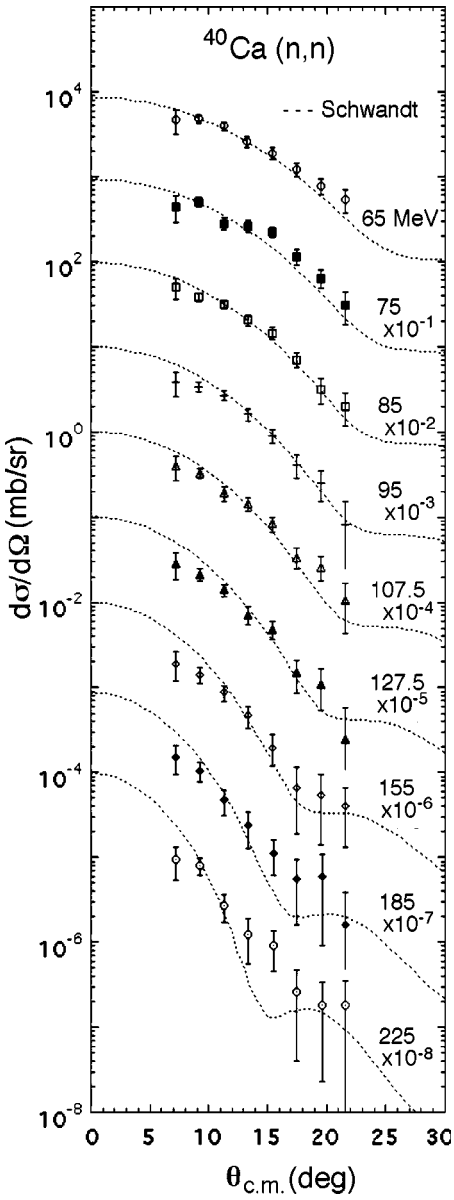


FIG. 11. Comparison of measured differential cross sections for $^{40}$Ca$(n,n)$ with predictions of Schwandt *et al.* [41] OMP.

The measured differential elastic cross sections over all energy bins are compared to the Schwandt phenomenological OMP predictions in Fig. 11, to the global Dirac phenomenological OMP predictions provided by Clark [18,43] in Fig. 12, and the predictions provided by Elster with Chinn's first-order microscopic OMP [44] in Fig. 13. Overall the data show fair agreement with both the Schwandt and Clark predictions with better large angle agreement with Clark at higher energies. The Elster predictions are generally below the 65 MeV data and appear to have too much diffraction; the local minima are too deep, although the limited angular resolution of our data could be a factor here. The data from the lowest angle are consistently lower than the predictions. As indicated in Sec. IV, the efficiency Monte Carlo calculation is very sensitive in this region. Slight inaccuracies in the geometry have a significant effect on the accuracy of the efficiency calculation. The data at energies less than 90 MeV at the larger angles are consistently higher than the predictions.

In Fig. 14 we compare the measurements with the more modern phenomenological global OMP predictions by Koning and Delaroche [40] and a semimicroscopic OMP developed by Bauge, Delaroche, and Girod [45]. The latter OMP is Lane consistent, and is built by folding radial matter densities from a Hartree-Fock-Bogoliubov calculation with a potential which is an extension of the one developed by Jeukenne, Lejeune, and Mahaux [46]. The data show fair agreement with both models for most energies, but agreement is less satisfactory for the lowest energies at larger angles.

### C. $^{208}$Pb$(n,n)$

The measurements of the $^{208}$Pb$(n,n)$ cross sections suffer from statistical uncertainties, particularly at the higher angles

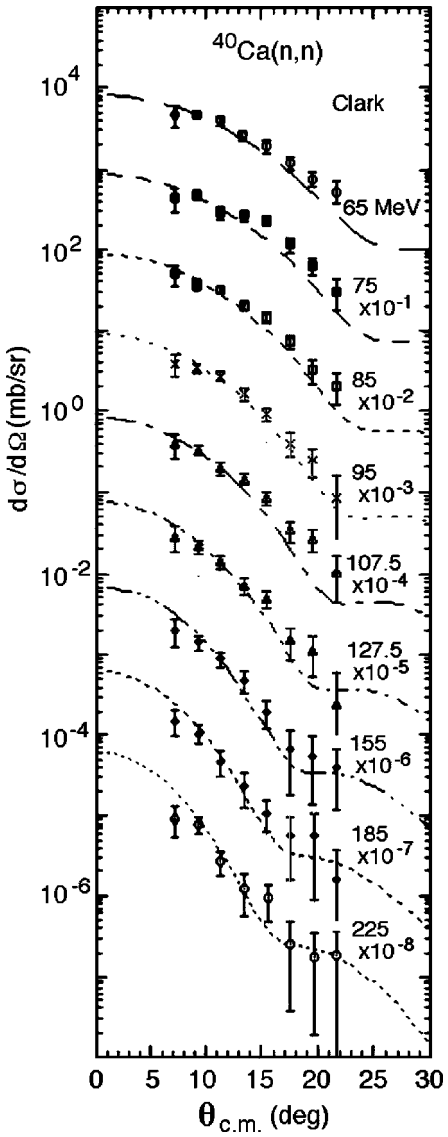


FIG. 12. Comparison of measured differential elastic cross sections for $^{40}$Ca($n,n$) with predictions of global Dirac phenomenology OMP provided by Clark [18,43].

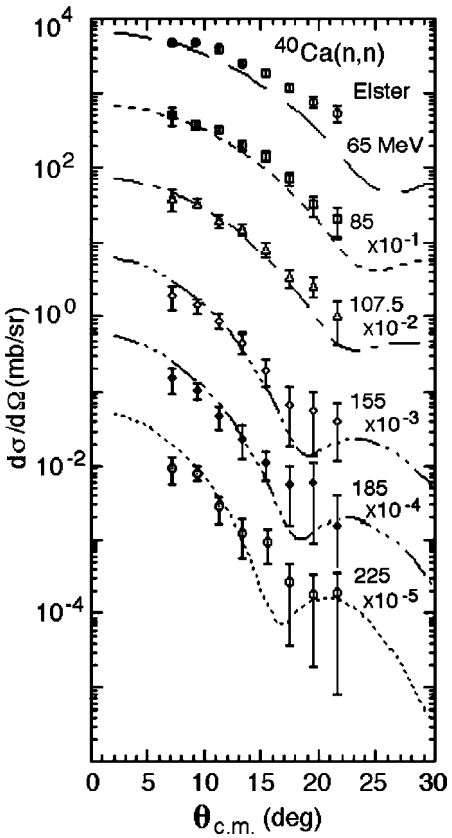


FIG. 13. Comparison of $^{40}$Ca($n,n$) data with predictions of microscopic OMP of Elster *et al.* [44].

and energies as can be seen in the excitation energy spectra shown in Fig. 5. The effect of changing incident neutron kinetic energy on the size of the elastic peak is demonstrated in Fig. 5(a) where the angular bin, $8<\theta_{nn}(\mathrm{lab})<10°$, is the same in each histogram. The 65 MeV histogram represents events where the scattered neutron converted to a proton in LC2 only while the other histograms contain data from both LC1 and LC2 conversions. The changes in the elastic peak as the neutron scattering angle is varied while maintaining the same incident energy bin ($80<E_{inc}<90$ MeV) is shown in Fig. 5(b). The Pb target-in to target-out spectra comparison is displayed in Fig. 5(c). The measured elastic differential cross sections for the $^{208}$Pb($n,n$) reaction are listed in Tables IX and X (Appendix B) along with their associated estimated errors.

The measured cross sections in the 65 MeV incident neutron energy bin are compared to previously published Pb($n,n$) cross sections at 65 MeV in Fig. 15(a). At forward angles the present data, the CNL data [3], and the more recent data of Ibaraki *et al.* [47,48] compare well. At larger angles uncertainties in the present data (due mainly to limited statistics) do not allow meaningful comparisons. In Fig. 15(b) the 95 MeV data are compared to 96 MeV data from Salmon [4] and Uppsala [6,7] and to the OMP predictions using the parameters reported in Ref. [41]. The agreement is satisfactory at most angles.

In Figs. 16, 17, 18, and 19 the experimental cross sections are compared with each of the OMP's used for the case of $^{40}$Ca described earlier. The error bars in these figures indicate combined systematic and statistical errors. As with the $^{40}$Ca($n,n$) data, the $^{208}$Pb($n,n$) model predictions are in fair agreement with the data. However, data uncertainties, particularly at the larger angles and energies, limit what can be concluded.

## V. CONCLUSIONS

Neutron differential elastic scattering cross sections have been measured for two $N=Z$ isotopes ($^{12}$C and $^{40}$Ca) and for one $N\neq Z$ isotope ($^{208}$Pb). The projectile neutron kinetic energy (mean bin value) ranged from 65 to 225 MeV while the center-of-mass scattering angle varied from 7° to 23°. At 65 MeV the data agree with earlier data from CNL [3], and more recent data of Ibaraki *et al.* [47,48]. The 95 MeV data, also over a limited angular range, agree with the 96 MeV Uppsala data [6,7] for $^{12}$C and $^{208}$Pb. The 96 MeV data from

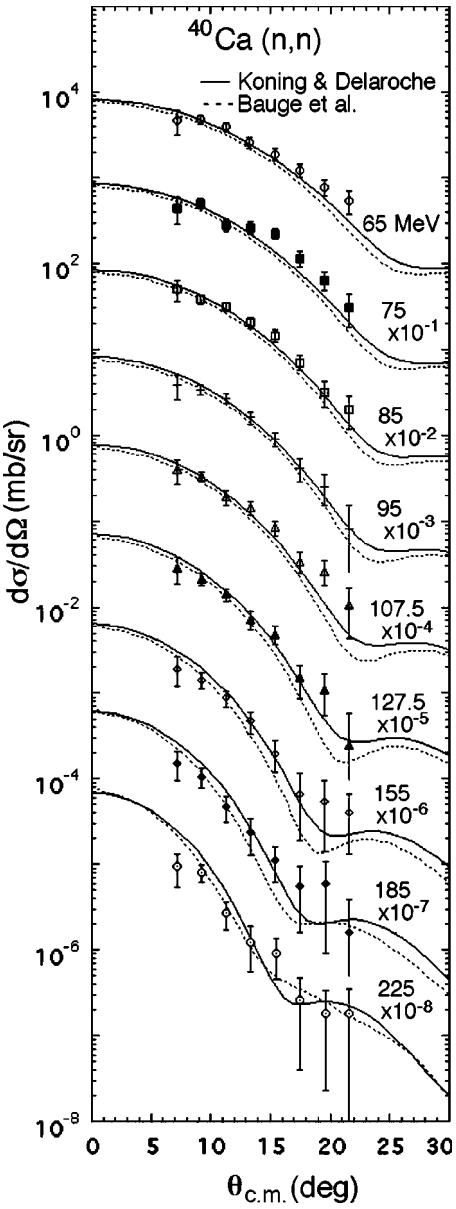


FIG. 14. Comparison of $^{40}$Ca$(n,n)$ data with phenomenological global OMP predictions by Koning and Delaroche [40] and a semimicroscopic OMP developed by Bauge, Delaroche, and Girod [45].

Salmon [4] for $^{12}$C falls, on average, about 20% below the Uppsala and the present data.

The measured $^{40}$Ca$(n,n)$ differential cross sections and the $^{208}$Pb$(n,n)$ differential cross sections have been compared to OMP predictions using the energy dependent parameters reported in Ref. [41], to the global Dirac phenomenological OMP predictions provided by Clark [18,43] and the predictions provided by Elster with Chinn's first-order microscopic OMP [44] with fair to good agreement over most of the data angular and energy ranges. The measured $^{12}$C$(n,n)$ differential cross sections were only compared with the Schwandt *et al.* and Comfort and Karp macroscopic OMP predictions with fair agreement over the middle energies.

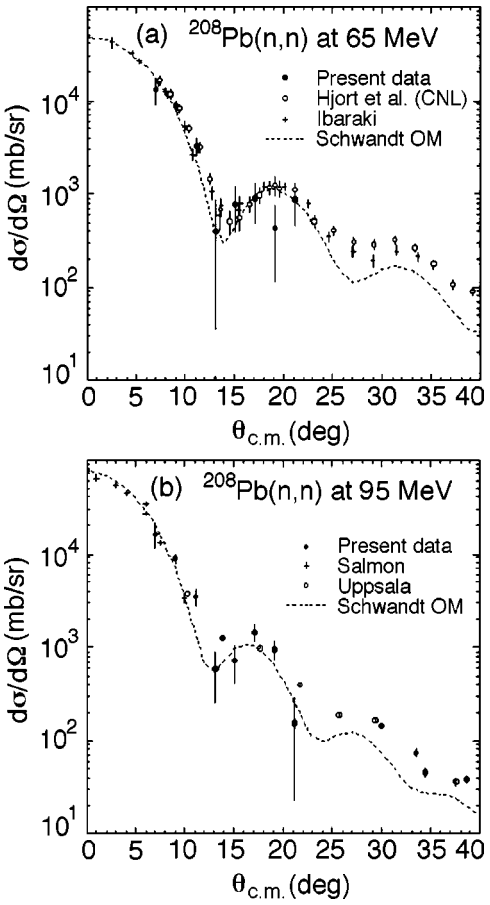


FIG. 15. (a) Comparison of $^{208}$Pb$(n,n)$ differential cross sections for $60 < E_{inc} < 70$ MeV from this experiment (filled circles) with the 65 MeV data taken at CNL at UC Davis [3] (open circles) and the more recent data of Ibaraki *et al.* [47,48]. Also shown is the Schwandt *et al.* [41] OM prediction at 65 MeV. (b) Comparison of $^{208}$Pb$(n,n)$ differential cross sections for $90 < E_{inc} < 100$ MeV from this experiment (filled circles) with data at 96 MeV from Salmon [4] (crosses) and, more recently, Uppsala [6,7] (open circles). Also shown is the Schwandt *et al.* [41] OM prediction at 95 MeV.

The measured $^{12}$C$(n,n)$, $^{40}$Ca$(n,n)$, and $^{208}$Pb$(n,n)$ differential cross sections have been compared to the modern global OMP prediction based on phenomenology by Koning and Delaroche [40] using the modern energy dependent parameters recently reported. The $^{40}$Ca$(n,n)$ and $^{208}$Pb$(n,n)$ differential cross sections have also been compared with a modern OMP based on microscopic nuclear theory using the Gogny D1S effective interaction folded with a Lane-consistent nuclear matter (based on an extension of the work reported in Ref. [45]).

The energy dependence of neutron elastic scattering reported here agree well with these modern model predictions, in particular in the energy dependence of the absolute differential cross sections. As noted earlier, there is interest in high energy neutron elastic scattering data, since the application of suitable models that adequately describe the data are used in a large number of applications. As described in more detail in Ref. [7], these applications are in nuclear medicine, nuclear energy, waste transmutation, and radiation effects on electronics.

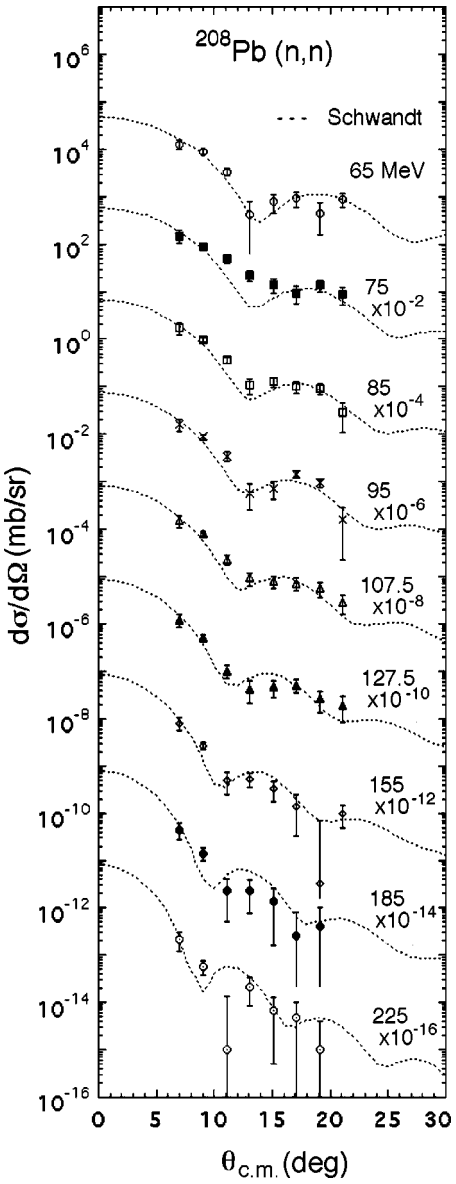


FIG. 16. Comparison of data for $^{208}$Pb$(n,n)$ with Schwandt *et al.* [41] OMP predictions.

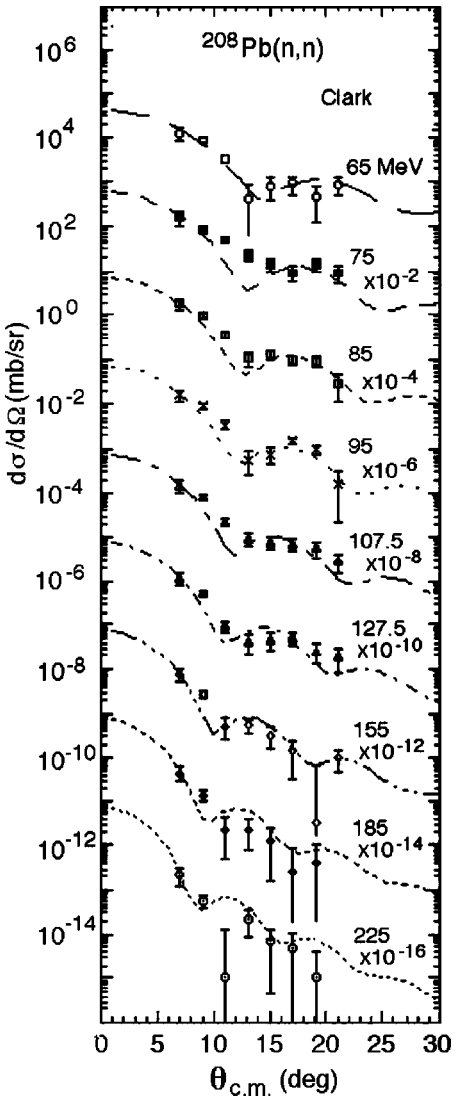


FIG. 17. $^{208}$Pb$(n,n)$ differential elastic cross sections compared with predictions by Clark [18,43] with the global Dirac phenomenological OMP.

These experiments have exploited a new technique applied with a continuum neutron beam to provide new neutron elastic scattering differential cross sections over a wide energy range. Overall these cross sections are in fair agreement with the predictions of models that were based mainly on proton elastic scattering data. The statistics and angular coverage of these results are limited, in part due to experimental and accelerator limitations at that time. However these first measurements over a wide energy range show the feasibility of this method.

## ACKNOWLEDGMENTS

This work has benefited from the use of the Los Alamos Neutron Science Center at the Los Alamos National Laboratory. This facility is funded by the U.S. Department of Energy and operated by the University of California under Contract No. W-7405-ENG-36. This work was also supported by the U.S. National Science Foundation under multiple grants and by the University of California.

## APPENDIX A: EFFICIENCY

### Definition of efficiency

Consider a small solid angle ($\Delta\Omega$) for neutron elastic scattering. Then Eq. (A1) can be used to calculate the experimental neutron elastic scattering differential cross section $d\sigma/d\Omega$:

$$N(E,\theta;E_{inc}) = I(E_{inc})N_t\frac{d\sigma}{d\Omega}F(E,\theta;\Delta\Omega). \qquad \text{(A1)}$$

In Eq. (A1), $N(E,\theta;E_{inc})$ is the number of neutrons detected with energy $E$, at scattering angle $\theta$ (with $\Delta\theta$ such that the solid angle subtended is $\Delta\Omega$), and with an incident neu-

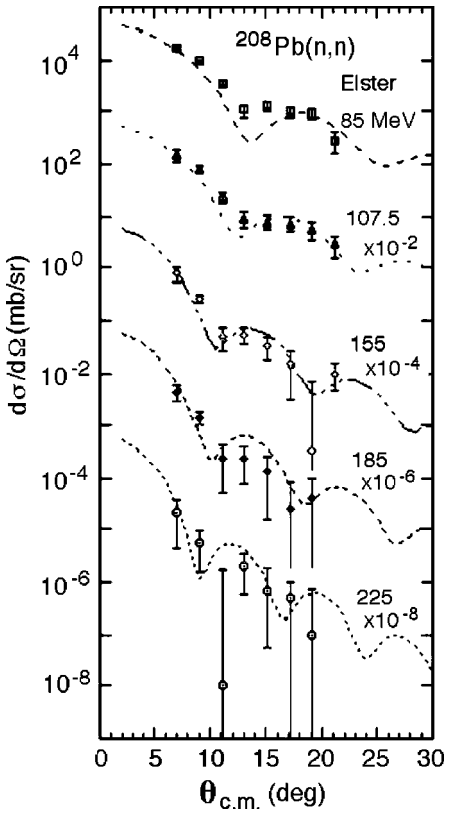


FIG. 18. $^{208}$Pb$(n,n)$ differential cross sections compared with predictions by Elster *et al.* [44].

tron energy of $E_{inc}$, $I(E_{inc})$ is the number of incident neutrons at $E_{inc}$, $N_t$ is the number of target atoms per cm$^2$, and $F(E,\theta;\Delta\Omega)$ is the efficiency factor to detect a neutron of energy $E$, at scattering angle $\theta$, into a solid angle $\Delta\Omega$.The definition of $F$ is shown in Eq. (A2):

$$F(E,\theta;\Delta\Omega) = \int \sum_{i=1}^{2} N_i \frac{d\sigma_H}{d\Omega}(\theta_i) d\Omega_i \cdot \Delta\Omega. \qquad \text{(A2)}$$

$N_1$ is the number of converter atoms per cm$^2$ in LC1, $(d\sigma_H/d\Omega)(\theta_1)$ is the lab $n$-$p$ differential cross section at angle $\theta_1$, and $\Omega_1$ is the solid angle subtended by the CsI detectors as seen by LC1, and similarly for LC2. Equation (A1) defines the efficiency factor $F$ while Eq. (A2) is integrated by the MC calculation to calculate $F$.

### Monte Carlo features

It is convenient to rewrite Eq. (A2) as Eq. (A3), where

$$Q_i(\theta_i,\Omega_i) = \int \frac{d\sigma_H}{d\Omega}(\theta_i) \frac{1}{\sigma_{el}(H)} d\Omega_i,$$

$$a = (N_1 + N_2) \cdot \sigma_{el}(H), \quad P_i = N_i \sigma_{el}(H)/a \ (i = 1,2),$$

$$F(E,\theta;\Delta\Omega) = [P_1 \cdot Q_1 + P_2 \cdot Q_2] \cdot a \cdot \Delta\Omega. \qquad \text{(A3)}$$

Since $P_1 + P_2 = 1$, the expression in brackets in Eq. (A3) states that the scattered neutron, once converted to a proton, does it in either LC1 or LC2 with probablities $P_1$ and $P_2$. After conversion, $Q_i(\theta_i,\Omega_i)$ is the probability that the proton will travel at angle $\theta_i$ into solid angle $\Omega_i$, where $i$ is either 1 or 2 for LC1 or LC2. Since both the total, $\sigma_{el}(H)$, and differential elastic $n$-$p$ cross sections are known, the MC simulation can calculate both the $P$ and $Q$ probabilities.

The MC is a three-dimensional simulation using relativistic kinematics [33]. The energy loss of converted protons along their flight path within the live converters and throughout the remainder of the detector telescope is calculated. The MC calculation can use either a point or an extended source of neutrons. (An extended source was used for the calculations for this experiment.) The effects of nuclear interactions within the CsI(Tl) detectors are included within the Monte

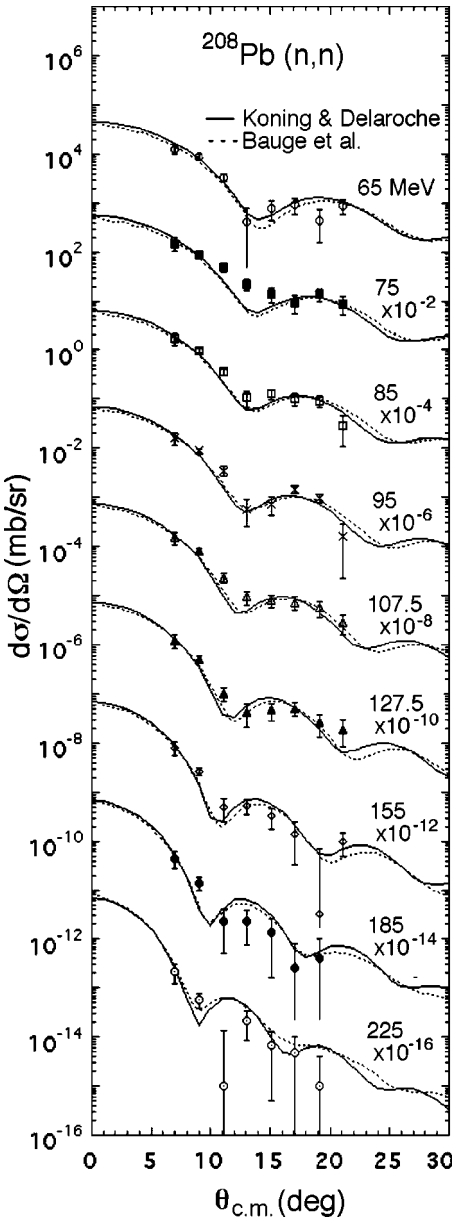


FIG. 19. Comparison of $^{208}$Pb$(n,n)$ data with phenomenological global OMP predictions by Koning and Delaroche [40] and a semimicroscopic OMP developed by Bauge, Delaroche, and Girod [45].

Carlo simulation. To simulate the conversion process, the MC simulation uses the Binstock *n-p* parametrization [49] for incident energies less than 100 MeV and uses the Arndt parametrization code [50] for incident energies greater than 100 MeV. The efficiencies calculated for 95 MeV using Binstock and Arndt agree within 3% on average. Recent *n-p* scattering data at 162 MeV from Uppsala [51] fall above partial wave analysis predictions (based on analyses of Refs. [51,52]) at the largest center-of-mass angles, i.e., those relevant to our MC conversion calculations. However, if we use a fit to those data the increase in conversion efficiency is only 1.6%. We do not include this change as the Uppsala data remain controversial.

The MC calculation converts $M$ neutrons (produced randomly in the target) to protons in either LC1 or LC2 at scattering angle $\theta$. Then each proton that arrives at the $E$ detector is counted and the total number of protons that make it to the $E$ detector is $H$. Then the efficiency factor is given by Eq. (A4):

$$F = \frac{H}{M} \cdot a \cdot 2\pi \sin(\theta) d\theta. \tag{A4}$$

To account for nuclear interactions within the CsI(Tl) crystals of the $E$ detector, $H$ is reduced by the appropriate energy dependent factor [31].

#### Other corrections

Before calculating the differential cross sections via Eq. (A1) it is necessary to consider corrections for the attenuation and multiple scattering of the beam and scattered flux into the detector. In general, the selection of target thicknesses was made so the different targets had similar attenuations and so net corrections for beam and scattered fluxes were relatively small compared to experimental uncertainties. The target attenuation of the beam flux $I$ into the fission chamber (beam flux monitor) is due to nuclear interactions governed by $\sigma_r$ and scatterings (governed by $\sigma_{sc}=\sigma_{el}$). Modifications of the beam flux attenuation are necessary because only part ($\approx 40\%$) of the beam flux into the fission chamber passes through the target. In addition to target attenuation of the scattered flux multiple scattering (MS) effects must be considered whereby flux is scattered into the detector above and beyond that due to single elastic scattering. For our targets the probability of MS is $\approx 10\%$ at 95 MeV, increasing by a few percent at 65 MeV and decreasing to 3–4 % at 200 MeV. The MS is angle dependent, being relatively larger at larger angles as compared to the single scattering distribution. Here we consider up to double scattering; triple scattering effects are estimated to be small—very much smaller than experimental uncertainties.

Consider, for example, the 95 MeV data for $^{40}$Ca$(n,n)$: The target attenuation flux loss for the area-weighted beam flux into the fission chamber is calculated to be 6.5%. The loss of neutron flux scattered into the detector is calculated to be 15% due to the target and 3.5% due to the detector system for neutrons and protons up to the latter entering the CsI(Tl) crystals. (Nuclear interaction losses in the crystals were considered separately earlier.) Multiple scattering corrections are calculated to be +8.5% at 7.2° and +14.5% at 21.6°. So the net correction for 95 MeV Ca decreases from $3.5\pm 4\%$ ($3.5 = -6.5+18.5-8.5$) at 7.2° to $-2.5\pm 4\%$ ($-2.5=-6.5+18.5-14.5$) at 21.6°. [The last three numbers in parentheses refer to corrections for (a) beam flux loss into the fission chamber, (b) scattered flux loss for the detector system, and (c) multiple scattering flux for the detector system.] The net corrections for $^{12}$Ca$(n,n)$ are similar, and as in the case for $^{40}$Ca, are smaller or much smaller than the combination of statistical and systematic uncertainties. Corrections at other energies are similar, with contributions, in general, decreasing with energy.

For $^{208}$Pb$(n,n)$ the situation is complicated by cross section minima, where MS corrections can be relatively large. At 95 MeV the net correction decreases from $4.5\pm 5\%$ at 7.8° ($4.5=-7+19-7.5$) to $-18\pm 8\%$ at the minimum near 13.1° ($-18=-7+19-30$) and then increases to $-2\pm 5\%$ at 21.1°. Corrections tend to increase at lower energies and decrease as one goes to higher energies. From Tables IX and X one can see that these corrections are, in general, much smaller than the experimental uncertainties.

## APPENDIX B: CROSS SECTION TABLES

Cross sections are shown in Tables V–X.


[1] S. M. Austin, in *Neutron-Nucleus Collisions: A Probe of Nuclear Structure*, edited by J. Rapaport, R. W. Finlay, S. M. Grimes, and F. S. Dietrich, AIP Conf. Proc. No. 124 (AIP, New York, 1985), p. 527.

[2] P. E. Hodgson, *The Optical Model of Elastic Scattering* (Clarendon Press, Oxford, 1963).

[3] E. Hjort, Ph.D. thesis, University of California, Davis, 1990; E. L. Hjort, F. P. Brady, J. L. Romero, J. R. Drummond, D. S. Sorenson, J. H. Osborne, B. McEachern, and L. F. Hansen, Phys. Rev. C **50**, 275 (1994).

[4] G. L. Salmon, Nucl. Phys. **21**, 15 (1960).

[5] J. Klug *et al.*, Nucl. Instrum. Methods Phys. Res. A **489**, 282 (2002).

[6] J. Klug *et al.*, Phys. Rev. C **67**, 031601(R) (2003).

[7] J. Klug *et al.*, Phys. Rev. C **68**, 064605 (2003).

[8] A. Bratenahl, S. Fernbach, R. H. Hildebrand, C. E. Leith, and B. J. Moyer, Phys. Rev. **77**, 597 (1950).

[9] R. H. Hildebrand, Lawrence Livermore National Laboratory Report UCRL 1169, 1951.

[10] W. P. Ball, Lawrence Livermore National Laboratory Report UCRL 1938, 1952.

[11] C. P. van Zyl, R. G. P. Voss, and R. Wilson, Philos. Mag. **1**, 1003 (1956).

[12] A. M. Lane, Nucl. Phys. **35**, 676 (1962).

[13] P. E. Hodgson, Rep. Prog. Phys. **47**, 613 (1984).
[14] J. Rapaport, J. D. Carlson, D. Bainum, T. S. Cheema, and R. W. Finlay, Nucl. Phys. **A286**, 232 (1977).
[15] J. Rapaport, Phys. Lett. **92B**, 233 (1980).
[16] L. G. Arnold, B. C. Clark, and R. L. Mercer, Phys. Rev. C **23**, 15 (1981); B. C. Clark (private communication).
[17] R. P. DeVito, S. M. Austin, U. E. P. Berg, R. DeLeo, and W. A. Sterrenburg, Phys. Rev. C **28**, 2530 (1983).
[18] B. C. Clark, in *Neutron-Nucleus Collisions: A Probe of Nuclear Structure* (Ref. [1]), p. 123.
[19] J. Rapaport, Phys. Rep. **87**, 25 (1982).
[20] P. W. Lisowski, C. D. Bowman, G. J. Russell, and S. A. Wender, Nucl. Sci. Eng. **106**, 208 (1990).
[21] J. L. Matthews, T. Akdogan, M. Chtangeev, W. A. Franklin, J. B. Hough, Y. Safkan, P. A. M. Gram, T. N. Taddeucci, J. L. Ullmann, and S. A. Wender, LANSCE Activity Report 1999–2000; Los Alamos National Laboratory Progress Report LA-13865-PR, 2001, p. 130.
[22] F. P. Brady, T. D. Ford, F. A. Needham, J. L. Romero, C. M. Castaneda, and M. L. Webb, Nucl. Instrum. Methods Phys. Res. A **228**, 89 (1984).
[23] T. D. Ford, G. A. Needham, F. P. Brady, J. L. Romero, and C. M. Castaneda, Nucl. Instrum. Methods Phys. Res. A **228**, 81 (1984).
[24] J. H. Osborne, J. L. Romero, F. P. Brady, E. L. Hjort, W. P. Caskey, J. C. Kintner, D. R. Mayo, D. S. Sorenson, and J. L. Ullmann, Nucl. Instrum. Methods Phys. Res. A **345**, 308 (1994).
[25] B. K. Park, Ph.D. thesis, Ohio University, 1991; Ohio University Report OU91-Accel-01, 1991 (unpublished).
[26] D. S. Sorenson, Ph.D. thesis, University of California, Davis, 1991; Los Alamos National Laboratory report LA-12061-T, 1991.
[27] A. Ling *et al.*, Phys. Rev. C **44**, 2794 (1991).
[28] R. L. Boudrie *et al.*, IEEE Trans. Nucl. Sci. **NS-26**, 4588 (1979).
[29] L. G. Atencio *et al.*, Nucl. Instrum. Methods Phys. Res. **187**, 381 (1981).
[30] C. L. Morris, Nucl. Instrum. Methods Phys. Res. **196**, 263 (1982).
[31] J. F. Janni, At. Data Nucl. Data Tables **27**, 147 (1982).
[32] S. A. Wender *et al.*, Nucl. Instrum. Methods Phys. Res. A **336**, 22 (1993).
[33] J. L. Romero, modification of computer program MAGPLT, (1995).
[34] P. Kunz, Computer code DWUCK4 (University of Colorado, unpublished).
[35] S. Kato *et al.*, Phys. Rev. C **31**, 1616 (1985).
[36] M. Buenard, Phys. Rev. C **13**, 444 (1976).
[37] H. Ejiri, M. Sasao, T. Shibata, H. Ohsumi, Y. Fujita, M. Fujiwara, T. Yamazaki, I. Katayama, S. Morinobu, and H. Ikegami, Phys. Rev. C **24**, 2001 (1981).
[38] Y. Fujita, M. Fujiwara, S. Morinobu, I. Katayama, T. Yamazaki, T. Itahashi, H. Ikegami, and S. Hayakawa, Phys. Rev. C **32**, 425 (1985).
[39] J. R. Comfort and B. C. Karp, Phys. Rev. C **21**, 2162 (1980).
[40] A. J. Koning and J. P. Delaroche, Nucl. Phys. **A713**, 231 (2003).
[41] P. Schwandt, H. O. Meyer, W. W. Jacobs, A. D. Bacher, S. E. Vigdor, M. D. Kaitchuck, and T. R. Donoghue, Phys. Rev. C **26**, 55 (1982).
[42] A. Nadasen, P. Schwandt, P. P. Singh, W. W. Jacobs, A. D. Bacher, P. T. Debevec, M. D. Kaitchuck, and J. T. Meek, Phys. Rev. C **23**, 1023 (1981).
[43] E. D. Cooper, S. Hama, B. C. Clark, and R. L. Mercer, Phys. Rev. C **47**, 297 (1993), and references therein.
[44] C. R. Chinn, C. Elster, and R. M. Thaler, Phys. Rev. C **48**, 2956 (1993); Ch. Elster (private communication).
[45] E. Bauge, J. P. Delaroche, and M. Girod, Phys. Rev. C **63**, 024607 (2001).
[46] J. P. Jeukenne, A. Lejeune, and C. Mahaux, Phys. Rev. C **16**, 80 (1977).
[47] M. Ibaraki, M. Baba, T. Miura, Y. Hirasawa, Y. Nauchi, H. Nakashima, S. I. Meigo, O. Iwamoto, and S. Tanaka, Nucl. Instrum. Methods Phys. Res. A **446**, 536 (2000).
[48] M. Baba, M. Ibaraki, T. Miura, T. Aoki, Y. Hirasawa, H. Nakashima, S. Meigo, and S. Tanaka, in Proceedings of the International Conference on Nuclear Data for Science & Technology, Tsukuba, edited by K. Shibata [J. Nucl. Sci. Technol., **Suppl 2**, 204 (2002)].
[49] J. Binstock, Phys. Rev. C **10**, 19 (1974).
[50] R. A. Arndt and L. D. Roper, Computer Code SCATTTERING ANALYSIS INTERACTION DIAL-IN (SAID) (SM88) (unpublished).
[51] C. Johansson *et al.*, J. Nucl. Sci. Technol., **Suppl 2**, 1406 (2002).
[52] J. J. de Swart and R. G. E. Timmermans, Phys. Rev. C **66**, 064002 (2002).